



**UNIVERSIDADE FEDERAL DO PARÁ
INSTITUTO DE GEOCIÊNCIAS
PROGRAMA DE PÓS-GRADUAÇÃO EM GEOLOGIA E GEOQUÍMICA**

DISSERTAÇÃO DE MESTRADO Nº 536

**A CONTRIBUIÇÃO DA LATERITIZAÇÃO NA FORMAÇÃO DO
MINÉRIO DE FERRO EM S11D - CARAJÁS**

Dissertação apresentada por:

ALINE CRISTINA SOUSA DA SILVA

Orientador: Prof. Dr. Marcondes Lima da Costa (UFPA)

**BELÉM
2018**

Dados Internacionais de Catalogação na Publicação (CIP)
Sistema de Bibliotecas da Universidade Federal do Pará
Gerada automaticamente pelo módulo Ficat, mediante os dados fornecidos pelo(a) autor(a)

S725c Sousa da Silva, Aline Cristina
A CONTRIBUIÇÃO DA LATERITIZAÇÃO NA FORMAÇÃO DO MINÉRIO DE FERRO EM S11D –
CARAJÁS / Aline Cristina Sousa da Silva. — 2018
x, 48 f. : il. color

Dissertação (Mestrado) - Programa de Pós-graduação em Geologia e Geoquímica (PPGG), Instituto de
Geociências, Universidade Federal do Pará, Belém, 2018.
Orientação: Prof. Dr. Marcondes Lima da Costa

I. Ferro. 2. Laterita. 3. Carajás, Serra dos (PA). I. Lima da Costa, Marcondes, *orient.* II. Título

CDD 551.072



**Universidade Federal do Pará
Instituto de Geociências
Programa de Pós-Graduação em Geologia e Geoquímica**

**A CONTRIBUIÇÃO DA LATERITIZAÇÃO NA FORMAÇÃO
DO MINÉRIO DE FERRO EM S11D – CARAJÁS**

DISSERTAÇÃO APRESENTADA POR:

ALINE CRISTINA SOUSA DA SILVA

**Como requisito parcial à obtenção do Grau de Mestre em Ciências na Área de
GEOQUÍMICA E PETROLOGIA**

Data de Aprovação: 24 / 07 / 2018

Banca Examinadora:

Prof. Dr. Marcondes Lima da Costa
Orientador - UFPA

Prof.ª Dr.ª Sonia Maria Barros de Oliveira
Membro - USP

Prof.ª Dr.ª Adriana Maria Coimbra Horbe
Membro - UnB

AGRADECIMENTOS

Ao meu orientador Professor Marcondes Lima da Costa pela paciência e dedicação.

Ao CNPq pelo financiamento da pesquisa e bolsa auxílio de mestrado.

A Vale pelo apoio logístico e financeiro.

Ao Programa de Pós-Graduação em Geologia e Geoquímica pelo suporte na pesquisa.

Aos laboratórios de Caracterização Mineral e de Microanálises do Instituto de Geociências UFPA.

Ao Professor Joel Buenano Macambira pela ajuda na descrição das lâminas petrográficas e discussões.

A Professora Vania Maria Barriga pela ajuda na descrição das lâminas petrográficas.

Ao Clovis Maurity pela ajuda, assistência, encorajamento e inúmeras discussões.

Ao Luiz Claudio Costa pela ajuda no campo, descrição e organização das amostras junto com o meu orientador.

Aos amigos que contribuíram para o trabalho: Lucélia Barros, Patrícia Rodrigues, Leonardo Boiadeiro, Pablo Santos, Darilena Porfírio e ao grupo de mineralogia e geoquímica aplicada por todo apoio e incentivo.

A minha família por todo o apoio emocional e financeiro.

Aos que não foram citados, mas contribuíram direta ou indiretamente para a realização desse trabalho, meu muito obrigada.

RESUMO

A origem do minério de ferro macio hospedado nos jaspilitos da Formação Carajás ainda é objeto de debate. A fim de contribuir para melhor compreensão de sua origem, o furo de sondagem SSDFD663 da mina de ferro S11D em Carajás foi investigado. Vinte amostras foram analisadas por DRX, microscopia óptica, química de rochas total e MEV/EDS. O perfil comprehende quatro horizontes de intemperismo, definidos da base ao topo, como protominério, saprolito grosso, saprolito fino e crosta. O minério principal ocorre distribuído ao longo do horizonte saprolítico, é composto principalmente por hematita e subordinadamente por magnetita. A quantidade de quartzo aumenta com a profundidade, enquanto que ao topo aumenta a quantidade de minerais de Fe-Al(Ti-P). O ferro total é enriquecido relativamente no saprolito fino em comparação com o protominério (42,55 a 97,62% em peso de Fe_2O_3). Os elementos traços, como Zr, Cr, Y e ETR, mostram aumento relativo em direção ao topo, uma vez que eles geralmente ocorrem na presença de minerais residuais (como zircão e anatásio). Além disso, os ETR exibem a assinatura geoquímica dos jaspilitos, o que reafirma sua relação genética. Sugere-se um modelo genético laterítico-supergênico para a origem do minério macio no depósito de S11D.

PALAVRAS-CHAVE: Jaspilito como protominério, perfil laterítico, minério de hematita.

ABSTRACT

The origin of the soft iron ore hosted in the jaspilites of the Carajás Formation is still subject of debate. In order to contribute to a better understanding of its origin, the SSDFD663 drill hole from the S11D iron mine in Carajás was investigated. Twenty samples were analyzed by XRD, optical microscopy, whole-rock chemistry and SEM/EDS. The profile comprises four weathering horizons, defined from the base to the top, such as protore, saprolite (coarse and fine), and crust. The main ore occurs distributed along the saprolite horizon, it is composed mainly of hematite, and subordinately by magnetite. The amount of quartz increases with the depth, while towards the top increases the amount of Fe-Al(Ti-P)-minerals. The total iron is enriched relatively in the fine saprolite in comparison to the protore (42.55 to 97.62 wt.% Fe_2O_3). Trace elements such as Zr, Cr, Y, and REE show relative enrichment upward since they usually occur in the presence of residual minerals (such as zircon and anatase). In addition, the REEs exhibit the geochemical signature of the jaspilites, which reaffirms their genetic relationship. A genetical laterite-supergene model is suggested for the origin of soft ore at the S11D deposit.

KEYWORDS: Jasplite-proto, lateritic profile, hematite ore.

LISTA DE ILUSTRAÇÕES

Figura 1- Localização dos depósitos de ferro em Carajás. Principais depósitos de ferro na Serra Norte (N1, N4 e N5), Serra Leste e Serra Sul (S11D). A) Brasil e o Cráton Amazônico; B) A Província Carajás. Fonte: USGS, modificado segundo os bancos de dados do IBGE e da CPRM.	1
Figure 2- Simplified geological map of Carajás. A) Brazil and the Amazon Craton; B) The Carajás Province. Source: Modified after Vasquez et al. (2008b).....	13
Figure 3- The geological cross section of the S11D mine, with main lithologies. The terms chemical canga, structural canga, and manganese iron ore are used in the mine geology in Carajás, being explained at the chapter “Profile of S11D deposit”. Source: Vale (unpublished data).	25
Figure 4- Simplified weathering profile and sample (20) locations of the S11D mine, Carajás.....	17
Figure 5- Mineralogy identified by XRD on the S11D samples. A) Jaspilite, black bands composed of hematite and magnetite, and light bands of jasper or chert; B) soft hematite, main composition is hematite (SEM micrography); C) hematite ore; D) ochreous goethite, probably aluminum-bearing; E) brown goethite, iron crust.....	18
Figure 6- Mineralogy of the lateritic profile on the S11D samples. A) magnetite (mt), jasper (jp) and carbonate (c); B) light bands of magnetite and dark bands of jasper; cross vein of carbonate with chalcopyrite (Cp); C-F) leached BIF; C) microplaty hematite (mpl), magnetite (mt) and quartz (qz); D-H) magnetite and pseudomorphic hematite after magnetite (psh); I) hematite with acicular radial brown goethite cement; J) detail of fig. I, acicular radial brown goethite; K-L) ochreous goethite and gibbsite (gb) in the crust. Photomicrographs under plane polarized light (A, E, I, K) and reflected light (B-L); micropores (p) are black.	20
Figure 7- Hematite ore. A-J) Pseudomorphic hematite after magnetite (psh); microplaty hematite (mpl); goethite (gt) cement. Photomicrographs of typical primary ore textures under reflected light.....	21

Figure 8- Box and whisker plot for the four major components of the 20 samples from S11D mine, Carajás. The full horizontal line is the median.	22
Figure 9- Chemostratigraphy of major and trace elements for 20 samples of S11D deposit. Noncontinuous lines are values under the detection limit.	24
Figure 10- Linear model bivariate of elements correlation of the S11D samples: A) Fe_2O_3 x SiO_2 ; B) P_2O_5 x Al_2O_3 ; C) TiO_2 x Al_2O_3 ; D) K_2O x MnO ; E) Hf x Zr ; F) Zr x TiO_2 . Horizons: CR – crust, FS – fine saprolite, CS – coarse saprolite, JP – jaspilite, M – mafic rock.	25
Figure 11- Chemical composition of the S11D samples normalized to the average values of the upper continental crust of the Earth after Rudnick and Gao, 2003. A) Samples. CR – crust; FS – fine saprolite; CS – coarse saprolite; JP – jaspilite; M – mafic rock.	26
Figure 11- (cont.) Chemical composition of the S11D samples normalized to the average values of the upper continental crust of the Earth after Rudnick and Gao, 2003. B) Median of samples in each horizon. CR – crust; FS – fine saprolite; CS – coarse saprolite; JP – jaspilite; M – mafic rock.	27
Figure 12- Chemical composition of the S11D samples normalized to the Carajás BIF average composition. Carajás BIF average composition after Macambira and Schrank, 2002; Macambira, 2003. A) Samples; B) Median of samples in each horizon. CR – crust; FS – fine saprolite; CS – coarse saprolite; JP – jaspilite; M – mafic rock.	28
Figure 13- Rare Earth Elements distribution normalized to chondrites after Barrat et al. (2012) of the S11D samples. A) Samples; B) Median of samples in each horizon. CR – crust; FS – fine saprolite; CS – coarse saprolite; JP – jaspilite; M – mafic rock.	29
Figure 14- Iron oxides dissolution textures. A-B) Jaspilite, euhedral light-colored crystals of magnetite and quartz (dark); B-C) fragments of opaque ancient banding and elongated porosity; D-F) crystals of pseudomorph hematite after magnetite and microplaty hematite; Photomicrographs on reflected light (A-B) and on SEM by retro-diffused electron (C-E) and secondary electron (F). Magnetite (mt), quartz (qz), pseudomorph hematite after magnetite (psh), goethite (gt), microplaty hematite (mpl) and porosity (p).	34

Figure 15- Iron oxides replacement textures. A-C) Concentric banding of fibrous, acicular to rods goethite crystals; C) the banding is concentric towards the porosity center; EDS microanalyses demonstrate variation on the layers composition, headed by Fe, Al and Si; D-E) pseudomorph hematite crystals after magnetite exhibit corroded bounders and sharp or rounded edges; D) goethite cement has filled the ghost crystals; E) most pseudomorph hematite crystals have been dissolved along preferential planes; F) EDS microanalyses of different dissolution stages of pseudomorph crystals demonstrate gradual input of Al depending on the amount of cement inside of the grain. Photomicrographs on plan polarized light (A), on reflected light (D) and on SEM by retro-diffused electron (B-C, E-F). Pseudomorph hematite after magnetite (psh), goethite (gt), and porosity (p). 36

Figure 16- Tri-plot (SiO_2 , Fe_2O_3 , Al_2O_3) of S11D samples data. Circle areas correspond to the determined range of BIF protore composition. Limits of lateritisation for typical laterite profile determined according to the calculation of Schellmann (1986). CR – crust; FS – fine saprolite; CS – coarse saprolite; JP – jaspilite; M – mafic rock. 37

Figure 17- Genesis model of lateritic-supergene iron ore in the Carajás Province. Magnetite (mt), quartz (qz), pseudomorph hematite after magnetite (psh), goethite (gt), microplaty hematite (mpl), and porosity (p). 40

SUMÁRIO

AGRADECIMENTOS	iv
RESUMO.....	v
ABSTRACT	vi
LISTA DE ILUSTRAÇÕES	vii
1 INTRODUÇÃO.....	1
1.1 APRESENTAÇÃO.....	1
1.2 JUSTIFICATIVA	2
2 OBJETIVOS.....	3
2.1 OBJETIVOS GERAIS	3
2.2 OBJETIVOS ESPECÍFICOS	3
3 ASPECTOS FISIOGRÁFICOS	4
3.1 RELEVO, VEGETAÇÃO E CLIMA.....	4
4 GEOLOGIA REGIONAL	5
5 MATERIAIS E MÉTODOS	7
5.1 AMOSTRAGEM.....	7
5.2 MINERALOGIA	7
5.3 COMPOSIÇÃO QUÍMICA TOTAL	8
6 THE CONTRIBUTION OF WEATHERING ON THE GENESIS OF THE IRON ORE AT S11D DEPOSIT, IN CARAJÁS, AMAZON REGION, BRAZIL	10
7 CONSIDERAÇÕES FINAIS	42
REFERÊNCIAS.....	43
ANEXO	47
ANEXO A - COMPROVANTE DE SUBMISSÃO AO "BRAZILIAN JOURNAL OF GEOLOGY"	48

1 INTRODUÇÃO

1.1 APRESENTAÇÃO

A Província Mineral de Carajás (PMC) é a maior província mineral brasileira e possui a maior reserva de minério de ferro de alto teor do mundo (mais de 65% Fe contido) (Grainger *et al.* 2008), estimada em 17 bilhões de toneladas (Vale 2017).

Os principais depósitos de ferro (fig. 1) em Carajás atualmente em fase de exploração são os de N5 (N5E e N5W), N4 (N4E, N4W, N4C) e S11D (Vale 2017), dos quais a produção total em 2017 foi de 169,2 milhões de toneladas (Vale 2018).

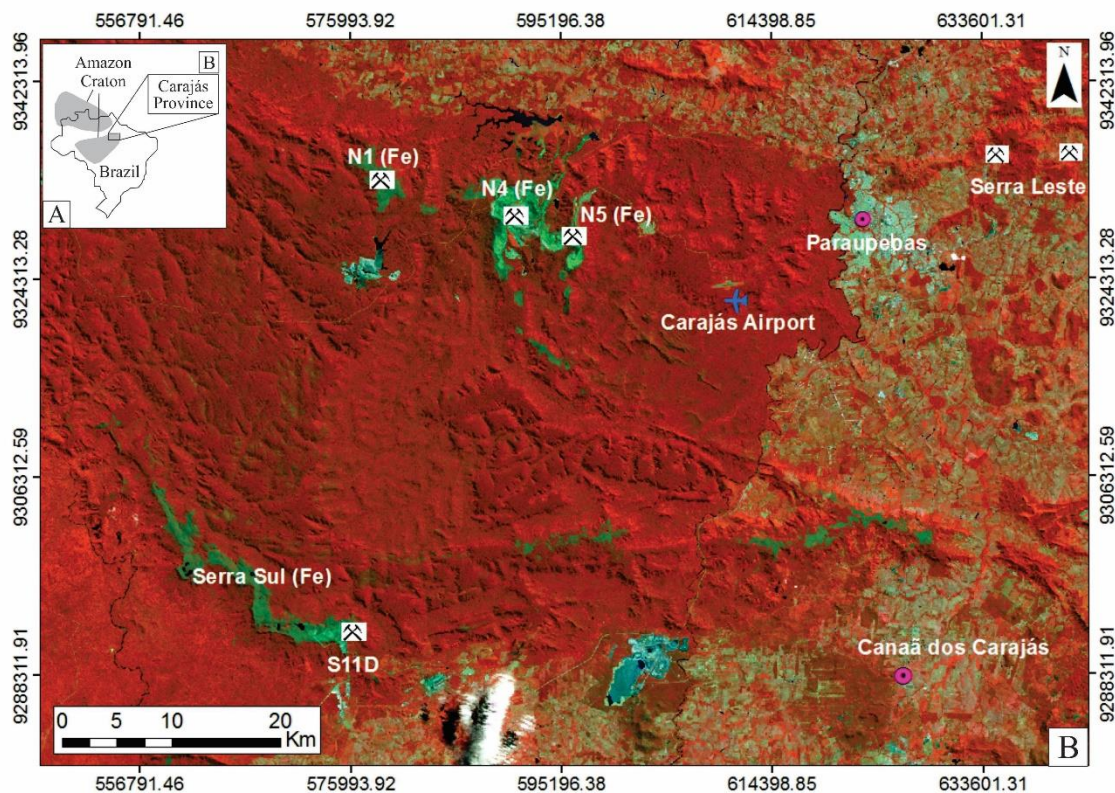


Figura 1- Localização dos depósitos de ferro em Carajás. Principais depósitos de ferro na Serra Norte (N1, N4 e N5), Serra Leste e Serra Sul (S11D). A) Brasil e o Cráton Amazônico; B) A Província Carajás. Fonte: USGS, modificado segundo os bancos de dados do IBGE e da CPRM.

Embora essa região tenha altos investimentos em exploração mineral, principalmente por parte da empresa Vale, o avanço do conhecimento geológico científico ainda é limitado, sendo necessários ainda estudos geológicos regionais e de detalhe que possam contribuir para o entendimento de sua complexa história geológica.

1.2 JUSTIFICATIVA

É notório que, a evolução dos processos genéticos na formação do minério de ferro em Carajás ainda é questionável. Dentre tantos fatores relevantes, destacam-se: a atuação do intemperismo sobre os jaspilitos e a contribuição metamórfica-hidrotermal sobre o produto da lixiviação intempérica. O primeiro fator foi o foco deste trabalho, enquanto que o segundo será apenas mencionado como resultado do atual contexto regional.

A origem laterítica para esses depósitos foi pouco estudada até o momento. O estudo dessas rochas é realizado na maioria dos casos por meio de furos de sondagem, devido à escassez de afloramentos e as restritas permissões de acesso à área, a qual a empresa Vale detém os direitos minerários. Isto dificulta em parte o estudo desses depósitos e o entendimento de sua evolução. O conjunto de trabalhos já desenvolvidos ainda não foi suficiente abrangente para a definição de um modelo genético regional, embora a PMC abrigue diversos depósitos comprovadamente de origem laterítica. Portanto, pretende-se com essa pesquisa contribuir para o melhor entendimento das características geológicas, mineralógicas e geoquímicas no depósito de S11D.

2 OBJETIVOS

2.1 OBJETIVOS GERAIS

O presente trabalho investigou a contribuição do intemperismo na formação do minério de ferro, no domínio da Serra Sul de Carajás, caracterizando do ponto de vista geológico, mineralógico e geoquímico o perfil laterítico, além de sua relação com o protominério (jaspilito) e possíveis rochas encaixantes, relacionadas as Formações Carajás e Parauapebas. Com isso, pretende-se sugerir a evolução do perfil de alteração intempérica desenvolvido sobre o protominério.

2.2 OBJETIVOS ESPECÍFICOS

Busca-se:

- caracterizar as fases minerais presentes em cada horizonte;
- estabelecer as relações geoquímicas dos minerais neoformados e herdados entre o perfil e a rocha mãe (jaspilito);
- propor a sucessão genética dos aspectos relacionados à textura, estrutura, grau de alteração e variações faciológicas;
- os processos que levaram à individualização dos horizontes;
- a relação genética e temporal entre os mesmos.

3 ASPECTOS FISIOGRÁFICOS

A área de estudo localiza-se na Província Mineral de Carajás, sudeste do estado do Pará, município de Canaã dos Carajás, Serra Sul.

3.1 RELEVO, VEGETAÇÃO E CLIMA

A Serra dos Carajás é parte do Domínio do Planalto Dissecado do Sul do Pará, caracterizado por maciços residuais de topo aplainado (platôs) e conjunto de cristas e picos interpenetrados por faixas de terrenos mais baixos (Radam 1974). Os platôs são alongados com margens escarpadas, com altitudes que variam entre 350 a 700 m (Ab'Saber 1986, Radam 1974).

Sobre os platôs, capeados por crosta, desenvolve-se vegetação arbustiva e gramíneas típica de cerrado, formando clareiras que contrastam com a floresta tropical adjacente (Secco & Mesquita 1983). Os platôs associados as rochas vulcânicas intemperizadas são cobertos por solos, onde se desenvolve a floresta pluvial densa (Pereira 1991).

O clima da região é tropical, quente e úmido (Aw - na classificação de Köppen), com temperaturas entre 19 e 31°C, com duas estações conhecidas na região: chuvosa, de novembro a abril; e seca, de maio a outubro (Schaefer *et al.* 2016). As médias pluviométricas variam de 1770 a 2.500 mm/ano, com umidade relativa de 52 a 98%, (médias em torno de 75%).

4 GEOLOGIA REGIONAL

A Serra dos Carajás se desenvolveu primordialmente sobre rochas do Supergrupo Itacaiúnas (Docegeo 1988), composto por sequências vulcânicas e sedimentares com idades entre 2,8 e 2,7 Ga, contexto no qual se encontra o Grupo Grão Pará (GGP) (Dall'Agnol *et al.* 2013, Grainger *et al.* 2008, Silva *et al.* 2014, Vasquez *et al.* 2008a).

O GGP é composto pelos jaspilitos da Formação Carajás, os quais ocorrem intercalados entre unidades metavulcânicas maficas, inferior e superior (Silva *et al.* 2014). A unidade metavulcânica inferior, atribuída à Formação Parauapebas, inclui metabasaltos amigdaloidais, porfiríticos, com lavas almofadadas e riolitos em derrames homogêneos, além de tuhos de *lapilli* e hialoclástos (Gibbs *et al.* 1986, Hirata *et al.* 1982). A unidade superior, pertencente à Formação Igarapé Cigarra, inclui metabasaltos com intercalações de tuhos recobertos por metassedimentos clásticos (arcósio e arenitos), formações ferríferas bandadas e chert (Silva *et al.* 2014). As duas unidades são interceptadas por diques e sills de gабro (Silva *et al.* 2014).

A Formação Carajás apresenta contatos concordantes e tectônicos com a rochas metavulcânicas, caracterizados por planos de falha com *slickensides* e desenvolvimento de foliação nas rochas metabásicas (Silva *et al.* 2014). Na área da Serra Norte, os jaspilitos são rochas finamente laminadas com estrutura plano paralela constituída por bandas alternadas de óxidos de ferro (hematita e magnetita), por jaspe e quartzo microcristalino (Lindenmayer *et al.* 2001, Macambira & Schrank 2002). Os jaspilitos exibem estruturas deposicionais preservadas tais como estruturas de escavação e preenchimento e esferulitos/grânulos de provável origem orgânica (Macambira 2003, Meirelles 1986).

Tolbert *et al.* (1971) consideraram pela primeira vez os jaspilitos como protominério do minério de ferro de Carajás, além de propor a origem do minério friável por meio de enriquecimento supergênico, após dissolução da sílica. Para Rosière & Chemale Jr (2000), a maior parte do minério de ferro de Carajás é representado pelo minério hematítico friável, com teor de 64 a 67 porcento de ferro. Na mina de N4E, por exemplo, os corpos de minério de alto teor ($> 65\%$ Fe) compõem de 100 a 400 m de espessura, e são interceptados por diques e *sills* de rochas maficas (Klein & Ladeira 2002).

Segundo Costa 1991, grande parte dos depósitos minerais e o substrato da paisagem desta região tiveram a contribuição da lateritização para sua formação. Estudos recentes propõem a contribuição do intemperismo laterítico ou alteração supergênica nas

rochas da região, como: Costa *et al.* (2009), Costa *et al.* (2011), Costa *et al.* (2014), Costa *et al.* (2016), Horbe & Costa (2005), Santos *et al.* (2016), Oliveira *et al.* (2016) baseados na intensa modificação causada pela lateritização e intensa atividade erosional que essas rochas foram submetidas (Costa *et al.* 2005). Vasconcelos *et al.* (1994) datou minerais de manganês formados sob condições de intemperismo laterítico em depósitos da região, provando que essas condições têm ocorrido desde pelo menos 70 Ma, de forma episódica, até o presente.

Além do minério hematítico friável, em Carajás também ocorre o minério de hematita dura ou minério compacto, em corpos tabulares ou lenticulares discordantes dentro do depósito de minério friável, concentrado próximo ao contato com as rochas metabásicas inferiores, e representam menos de 10 % dos recursos (Dalstra & Guedes 2004).

Segundo Figueiredo e Silva *et al.* (2013), a contribuição hidrotermal para a formação do minério compacto é caracterizada pela recristalização de jaspe, remoção do Fe e formação de magnetita sobrecrecida a hematita microcristalina, associada a quartzo e veios carbonáticos (Dalstra & Guedes 2004, Figueiredo e Silva *et al.* 2008, Figueiredo e Silva *et al.* 2011). O minério compacto, no entanto, não será abordado neste trabalho.

5 MATERIAIS E MÉTODOS

5.1 AMOSTRAGEM

Para a realização do presente trabalho o Prof. Dr. Marcondes Lima da Costa (IG-UFPA) e o Msc. Luiz Claudio Costa (Vale) descreveram diversos furos de sondagem na casa de testemunhos da Vale, em outubro de 2015, com posterior coleta de amostras representativas dos perfis laterítico. Ao fim das seções de descrição, 55 amostras foram selecionadas para análises do testemunho de sondagem SSDFD663, que alcançou 524,5 m com inclinação de -84,84°, na direção de 165,38°, localizado sob as coordenadas UTM 576.320.847/9.292.204,02 na mina de ferro de S11D. As amostras coletadas foram representativas das diferentes zonas ou horizontes do perfil de alteração laterítica. As amostras foram descritas em escala macro- e mesoscópica e fotografadas. Vinte amostras foram selecionadas para análises mineralógicas e químicas.

5.2 MINERALOGIA

Para a identificação mineralógica, empregou-se a difratometria de raios x (DRX), microscopia óptica e microscopia eletrônica de varredura com sistema de análise por energia dispersiva (MEV/EDS). Os equipamentos utilizados nas três técnicas pertencem ao Instituto de Geociências da UFPA (IG-UFPA).

A mineralogia foi determinada por DRX, aplicando-se o método do pó. O equipamento utilizado foi um difratômetro de raios x, modelo Empyrean da PANalytical, com tubos de raios-X cerâmico de anodo de Co ($K_{\alpha 1} = 1,789010 \text{ \AA}$), foco fino longo, filtro K_{β} de Fe, detector PIXCEL3D-Medpix3 1x1, no modo *scanning*, com voltagem de 40 kV, corrente de 35mA, tamanho do passo $0,0263^{\circ}$ em 2θ , varredura de 4° a 75° em 2θ , tempo/passo de 30,6 s, fenda divergente: $1/4^{\circ}$ e anti-espalhamento: $1/2^{\circ}$, máscara: 10 mm. O equipamento pertence ao Laboratório de Caracterização Mineral (IG-UFPA). A aquisição dos dados foi realizada através do software X’Pert Data Collector, versão 2.1a, e o tratamento dos dados com X’Pert HighScore versão 2.1b.

A caracterização mineral foi complementada por microscopia óptica, utilizando seis seções polidas e catorze lâminas delgadas polidas, preparadas na oficina de laminação do IG-UFPA. As seções polidas foram estudadas por microscopia de luz refletida com o objetivo de observar as relações mineralógicas, texturais e estruturais dos minerais opacos. Da mesma forma as lâminas delgadas foram investigadas por microscopia, empregando-se os métodos de luz transmitida e refletida. Para isso, utilizou-se o microscópio ótico da marca Laica, modelo DM 2700P pertencente ao laboratório de Gemologia do IG-UFPA.

As microfotografias foram obtidas com câmera acoplada da marca Laica, modelo MC170 HD. As imagens utilizadas no trabalho foram obtidas utilizando filtro cinza, sob: luz transmitida (nicóis paralelos e cruzados) e luz refletida (nicóis paralelos e cruzados).

A Microscopia Eletrônica de Varredura (MEV) foi utilizada para observar as características morfológicas e texturais do minério de ferro e rochas associadas em escala micrométrica. O equipamento utilizado foi o MEV modelo LEO-1430 pertencente ao Laboratório de Microanálises do IG-UFPa. As condições de análise para as imagens de elétrons secundários foram: corrente do feixe de elétrons = $90\mu\text{A}$, voltagem de aceleração constante = 10 kV, distância de trabalho = 15 mm. Os princípios gerais de funcionamento do MEV são descritos em Reed (1996). Essas análises foram realizadas sob fragmentos centimétricos das amostras in natura, fixados sobre o suporte do equipamento com fita de carbono dupla face, utilizando o método de elétrons secundários. Sob as lâminas delgadas polidas e seções polidas foi aplicado o método de elétrons retroespalhados. Em ambos os métodos a metalização utilizada foi com ouro. As fases minerais de maior interesse foram analisadas por espectrometria de energia dispersiva de raios-x (EDS).

5.3 COMPOSIÇÃO QUÍMICA TOTAL

As análises químicas de amostra total foram realizadas pelos Laboratórios da ALS. Os elementos maiores foram determinados por fluorescência de raios-x (FRX), após fusão com metaborato ou tetraborato de lítio, utilizando o método ME-XRF26; os elementos menores foram determinados por ICP-MS, utilizando o método ME-MS41, após digestão por água régia; os terras raras e elementos traços foram determinados por ICP-MS, após fusão com borato de lítio, utilizando o método ME-MS81U. Cl e F foram determinados por cromatografia iônica (Cl-IC881, F-IC881). Carbono e enxofre total foram determinados por forno Leco e espectroscopia de infravermelho (C-IR07, S-IR08). Os métodos de análise química utilizados para cada elemento (segundo as referências da ALS) e os seus respectivos limites de detecção são apresentados na tabela 1.

Tabela 1- Métodos de análise química utilizados para cada elemento segundo as referências da ALS e os respectivos limites de detecção (mínimo e máximo); óxidos expressos em % e elementos menores e traços em ppm. Os elementos foram organizados em ordem alfabética.

Óxidos	Min. (%)	Máx. (%)	Ref. ALS	Elem.	Min. (ppm)	Máx. (ppm)	Ref. ALS	Elem.	Min. (ppm)	Máx. (ppm)	Ref. ALS
Al₂O₃	0,01	100	ME-XRF26	Ag	0,01	100	ME-MS41	Na	0,01%	10%	ME-MS41
BaO	0,01	66	ME-XRF26	Al	0,01	25%	ME-MS41	Nb	0,05	500	ME-MS41
CaO	0,01	60	ME-XRF26	As	0,1	10	ME-MS41	Nb	0,2	2,5	ME-MS81U
Cr₂O₃	0,01	10	ME-XRF26	Au*	0,2	25	ME-MS41	Nd	0,1	10	ME-MS81U
Fe₂O₃	0,01	100	ME-XRF26	B	10	10	ME-MS41	Ni	0,2	10	ME-MS41
K₂O	0,01	15	ME-XRF26	Ba	10	10	ME-MS41	P	10	10	ME-MS41
MgO	0,01	50	ME-XRF26	Ba	0,5	10	ME-MS81U	Pb	0,2	10	ME-MS41
MnO	0,01	39	ME-XRF26	Be	0,05	1	ME-MS41	Pr	0,03	1	ME-MS81U
Na₂O	0,01	10	ME-XRF26	Bi	0,01	10	ME-MS41	Rb	0,1	10	ME-MS41
P₂O₅	0,01	46	ME-XRF26	C	0,01%	50%	C-IR07	Rb	0,2	10	ME-MS81U
SO₃	0,01	34	ME-XRF26	Ca	0,01%	25%	ME-MS41	Re	0,001	50	ME-MS41
SiO₂	0,01	100	ME-XRF26	Cd	0,01	1	ME-MS41	S	0,01%	10%	ME-MS41
SrO	0,01	1,5	ME-XRF26	Ce	0,02	500	ME-MS41	S	0,01%	50%	S-IR08
TiO₂	0,01	30	ME-XRF26	Ce	0,5	10	ME-MS81U	Sb	0,05	10	ME-MS41
PF	0,01	100	OA-GRA05x	Cl	50	20,000	Cl – IC881	Sc	0,1	10	ME-MS41
				Co	0,1	10	ME-MS41	Se	0,2	1	ME-MS41
				Cr	1	10	ME-MS41	Sm	0,03	1	ME-MS81U
				Cr	10	10	ME-MS81U	Sn	0,2	500	ME-MS41
				Cs	0,05	500	ME-MS41	Sn	1	10	ME-MS81U
				Cs	0,01	10	ME-MS81U	Sr	0,1	10	ME-MS81U
				Cu	0,2	10	ME-MS41	Sr	0,2	10	ME-MS41
				Dy	0,05	1	ME-MS81U	Ta	0,01	500	ME-MS41
				Er	0,03	1	ME-MS81U	Ta	0,1	2,5	ME-MS81U
				Eu	0,03	1	ME-MS81U	Tb	0,01	1	ME-MS81U
				F	20	20,000	F – IC881	Te	0,01	500	ME-MS41
				Fe	0,01%	50%	ME-MS41	Tm	0,01	1	ME-MS81U
				Ga	0,05	10	ME-MS41	Th	0,2	10	ME-MS41
				Ga	0,1	1	ME-MS81U	Th	0,05	1	ME-MS81U
				Gd	0,05	1	ME-MS81U	Ti	0,005%	10%	ME-MS41
				Ge	0,05	500	ME-MS41	Tl	0,02	10	ME-MS41
				Hf	0,02	500	ME-MS41	U	0,05	10	ME-MS41
				Hf	0,2	10	ME-MS81U	U	0,05	1	ME-MS81U
				Hg	0,01	10	ME-MS60	V	1	10	ME-MS41
				Ho	0,01	1	ME-MS81U	V	5	10	ME-MS81U
				In	0,005	500	ME-MS41	W	0,05	10	ME-MS41
				K	0,01%	10%	ME-MS41	W	1	10	ME-MS81U
				La	0,2	10	ME-MS41	Y	0,05	500	ME-MS41
				La	0,5	10	ME-MS81U	Y	0,5	10	ME-MS81U
				Li	0,1	10	ME-MS41	Yb	0,03	1	ME-MS81U
				Lu	0,01	1	ME-MS81U	Zn	2	10	ME-MS41
				Mg	0,01%	25%	ME-MS41	Zr	0,5	500	ME-MS41
				Mn	5	50	ME-MS41	Zr	2	10	ME-MS81U
				Mo	0,05	10	ME-MS41				

6 THE CONTRIBUTION OF WEATHERING ON THE GENESIS OF THE IRON ORE AT S11D DEPOSIT, IN CARAJÁS, AMAZON REGION, BRAZIL

Aline Cristina Sousa da Silva & Marcondes Lima da Costa

(Manuscrito submetido ao “Brazilian Journal of Geology”)

ABSTRACT

The origin of the soft iron ore hosted in the jaspilites of the Carajás Formation is still subject of debate. In order to contribute to a better understanding of its origin, the SSDFD663 drill hole from the S11D iron mine in Carajás was investigated. Twenty samples were analyzed by XRD, optical microscopy, whole-rock chemistry and SEM/EDS. The profile comprises four weathering horizons, defined from the base to the top, such as protore, saprolite (coarse and fine), and crust. The main ore occurs distributed along the saprolite horizon, it is composed mainly of hematite, and subordinately by magnetite. The amount of quartz increases with the depth, while towards the top increases the amount of Fe-Al(Ti-P)-minerals. The total iron is enriched relatively in the fine saprolite in comparison to the protore (42.55 to 97.62 wt.% Fe₂O₃). Trace elements such as Zr, Cr, Y, and REE show relative enrichment upward since they usually occur in the presence of residual minerals (such as zircon and anatase). In addition, the REEs exhibit the geochemical signature of the jaspilites, which reaffirms their genetic relationship. A genetical laterite-supergene model is suggested for the origin of soft ore at the S11D deposit.

KEYWORDS: Jaspilite-protoore, lateritic profile, hematite ore.

INTRODUCTION

The Carajás Province (CP) is the largest Brazilian mineral province, estimated at 17 billion tons (Vale 2017), holding the largest reserves of high-grade iron ore in the world (Grainger *et al.* 2008). The main iron deposits currently under exploitation are those of N5 (N5E and N5W), N4 (N4E, N4W, N4C) and S11D (Vale 2017). In 2017, the total production of iron ore in Carajás was amounted to 169.2 million tons (Vale 2018).

Although this region has high investments in mineral exploration, mainly by the Vale company, the advance of scientific geological knowledge is still limited, being necessary regional and detailed geological studies to contribute to the understanding of its complex geological history.

The present work has investigated the geological, mineralogical, and geochemical characteristics of a lateritic profile at Serra Sul, southeast of Pará state, Brazil (fig. 2), where the S11D iron mine is located. The reserves of iron ore at Serra Sul are estimated at 4.24 billion tons, within more than 66.7 wt.% Fe content (Vale 2017).

The primary aim was a characterization of the mineralogy in each horizon, to measure a relationship between the ores and protore (jaspilite). Using the geochemistry to state again as a fact the affinity between the newly formed and inherited minerals. Proposing a genetic sequence for textures, structures, weathering degree, and faciological variations, along with the processes that led to the individualization of horizons. At long last suggesting an evolution of the lateritic-supergene profile.

GEOLOGICAL SETTINGS

The iron deposits are hosted on jaspilites (banded iron formation - BIF) of the Carajás Formation, an intermediate unit of the Grão Pará Group (GPG, fig. 2 and 3). On its contact below, occurs the Parauapebas Formation (basalts and rhyolites), and over-leaping it mafic and sedimentary rocks of Igarapé Cigarra Formation (Dall'Agnol *et al.* 2013, Grainger *et al.* 2008, Silva *et al.* 2014, Vasquez *et al.* 2008a). The contacts between them are concordant and tectonics (Silva *et al.* 2014).

The jaspilites are characterized by irregular and discontinuous intercalations of millimetric mesobands of chert with hematite dust (i.e. jasper) and iron oxides bands, showing primary and depositional structures (Lindenmayer *et al.* 2001, Macambira & Schrank 2002). The content of iron on BIF ranges from 17.11 to 43.40 wt.% Fe and 35.10 to 60.84 wt.% Si (Meirelles 1986). A volcanogenic origin for these jaspilites is indicated by Darlenne & Schobbehaus (2001), Klein & Ladeira (2002), and Meirelles (1986), based on the GPG environment and/or the geochemical characteristics of the jaspilites (Figueiredo e Silva *et al.* 2011).

There are two types of hematite ores hosted in the Carajás Formation, the soft (i.e. high porosity) and the hard (i.e. low porosity). The soft hematite ore represents most of iron ore in Carajás, with 64 to 67 percent of iron content (Rosière & Chemale Jr 2000). At the N4E mine, for example, the high-grade ore bodies have composed 100 to 400 m thick, intercepted by dykes and sills of mafic rocks (Klein & Ladeira 2002). This ore was considered by Tolbert *et al.* (1971) as a product of supergenic enrichment after dissolution of the silica.

According to Costa (1991), a great part of the mineral deposits and the substrate of the landscape of this region had the contribution of lateritisation to its formation. The contribution of laterite weathering or supergenic alteration, over the ore deposits in Carajás and in the Amazon region, have been studied by Costa *et al.* (2009), Costa *et al.* (2011), Costa *et al.* (2014), Costa *et al.* (2016), Horbe & Costa (2005), Santos *et al.* (2016), and Oliveira *et al.* (2016), based on the intense modification that these rocks and others have undergone by the lateritisation and intense erosional activity (Costa et al., 2005a). Vasconcelos et al. (1994) dated manganese minerals formed under conditions of lateritic weathering in deposits of the region, proving that these conditions have occurred from at least 70 Ma, episodically, to the present.

The hard iron ore has tabular or lenticular shape, discordant within the soft ore deposit, concentrated near the contact with the lower metabasic rocks, and represent less than 10% of the resources (Dalstra & Guedes 2004). The hydrothermal contribution to the formation of the hard ore is characterized by jasper recrystallization, removal of Fe and formation of magnetite crossed over with microcrystalline hematite, associated with quartz and carbonate veins (Figueiredo e Silva *et al.* 2008, Figueiredo e Silva *et al.* 2013).

The hard ore will not be discussed in this paper.

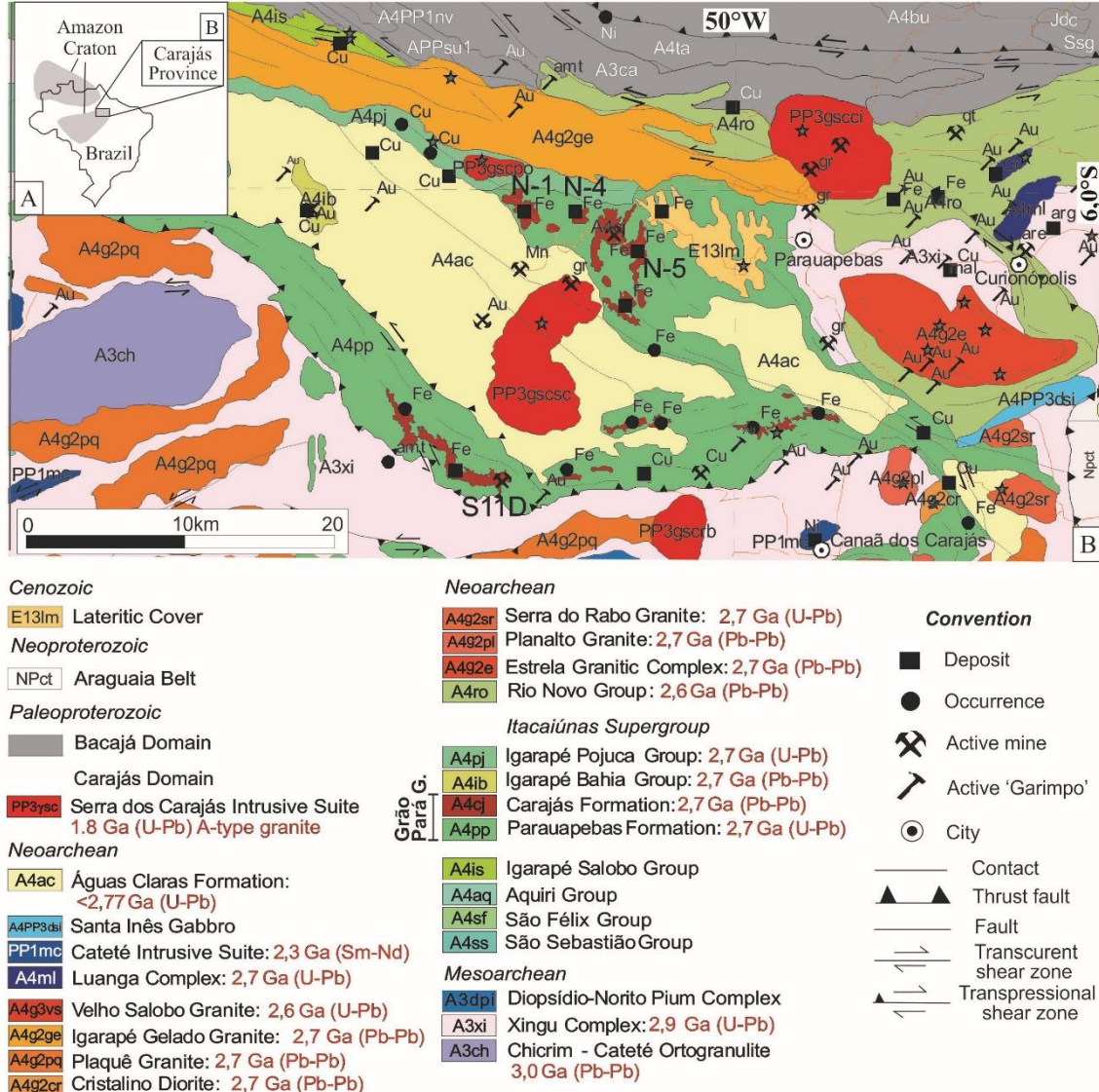


Figure 2- Simplified geological map of Carajás. A) Brazil and the Amazon Craton; B) The Carajás Province. Source: Modified after Vasquez *et al.* (2008b).

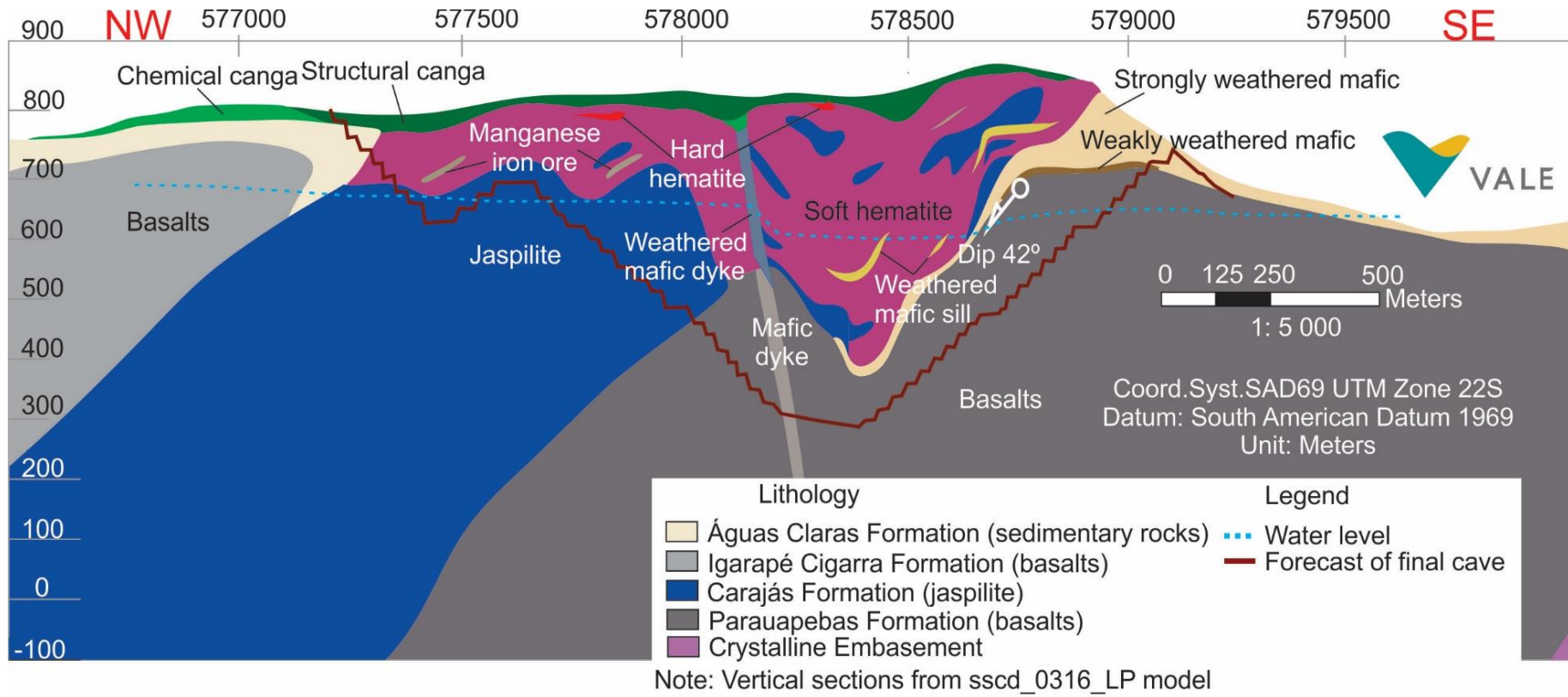


Figure 3- The geological cross section of the S11D mine, with main lithologies. The terms chemical canga, structural canga, and manganese iron ore are used in the mine geology in Carajás, being explained at the chapter “Profile of S11D deposit”. Source: Vale (unpublished data).

MATERIALS AND METHODS

This research involves years of field geology carried out in the iron ore mines of Carajás, and description of drill holes by the second author. For this paper, one drill hole (SSDFD663) was selected comprising 524.5m (-84.84°/165.38° direction), positioned at the S11D iron mine (UTM 576.320.847/9292204.02). In total, fifty-five samples were collected at different depths from the most weathered to the freshest rock. Only twenty samples were analyzed by optical microscopy, X-ray diffraction (XRD), X-ray fluorescence (XRF), inductively coupled plasma mass spectrometry (ICP-MS), and scanning electron microscope coupled with an energy-dispersive X-ray spectroscopy (SEM/EDS).

The mineralogy was determined by XRD on powdered samples (with CoK α radiation and Fe K β filter on a Panalytical Emryean); supported by optical microscopy (with a Leica model DM 2700P) on polished mounts and thin sections - the images used were obtained using gray filter; SEM/EDS (Zeiss LEO 1430 with 500 DP XSD from IXRF-4 Systems Inc) was used on small fragments, thin sections and polished mounts, applying secondary and retro-diffused electron detector methods.

The whole-rock chemistry was determined by ALS Ltda (Belo Horizonte, Brazil) on the twenty pulp samples. Major elements were analyzed by XRF, after lithium metaborate or tetraborate fusion (by ME-XRF26 group method); the minor elements by ICP-MS, after digestion by Aqua Regia (ME-MS41), gold determinations by this method are semi-quantitative due to the small sample weight used (0.5g); the rare earth and trace elements were determined by ICP-MS, after lithium borate fusion (ME-MS81U); Cl and F by ion chromatography (Cl-IC881, F-IC881); carbon and total sulfur by Leco furnace and infrared spectroscopy (C-IR07, S-IR08); loss on ignition (LOI) by calcination (OA-GRA05x). The chemical analysis methods used for each element according to the ALS references and respective detection limits are showing in table 1.

The measured REE contents were normalized to Chondrites (Barrat *et al.*, 2012). The relative enrichment and depletion of Eu and Ce were evaluated according to the Eu/Eu* and Ce/Ce* ratios defined as (McLennan, 1989): $\text{Eu/Eu}^* = \text{Eu}_N / (\text{Sm}_N \cdot \text{Gd}_N)^{0.5}$ and $\text{Ce/Ce}^* = 5\text{Ce}_N / (4\text{La}_N) + (\text{Sm}_N)$, where the subscript N denotes the chondrite-normalized value and Eu* represents the Eu value expected for a smooth chondrite-normalized REE pattern. Eu/Eu* values are good indicators of source-rock composition (McLennan 1989).

PROFILE OF THE S11D DEPOSIT

MESOSCOPIC CLASSIFICATION OF THE IRON ORE PROFILE

Typical weathering horizons were developed along the drill hole SSDFD663, as (fig. 4): protore (525-460m), coarse saprolite (459-230m), fine saprolite (229-31m) and crust (30m).

The jaspilites represent the protore of the weathering profile, occurring at its base. They show meso-microbands of dominant magnetite, and hematite (fig. 5A), parallel-banded with jasper/chert, which may contain quartz or carbonate veins with copper minerals, as chalcopyrite (fig. 6A-B). The veins of carbonate are most dolomitic (fig. 6B). On the depth of 515m, interbedded with jaspilite occurs a “mafic”-carbonate rock composed of chlorite, biotite, calcite, quartz, magnetite, chalcopyrite, pyrite, hematite and tourmaline.

The coarse saprolite (CS) horizon is most composed of a high-grade hematite ore, which commonly shows centimeter-size prisms-plates, defined by joint planes and fissile beds, which may display primary lamination. The ore can be classified in terms of hardness, such as: soft or powdery/dusty (fig. 5B). Soft ore shows high amount of hematite, gray color, metallic luster and high porosity, being composed of pseudomorphic hematite after magnetite (psh) and microplaty hematite (mpl), with quartz as accessory (fig. 5C). Locally, the dusty ore may have a few amounts of manganese oxy-hydroxides (“manganese iron ore”), as cryptomelane or hollandite. The CS can locally exhibit weathered fragments of jaspilite with medium to low amount of quartz (fig. 7).

The fine saprolite (FS) is characterized by dominance of soft ore, with fine grained to massive hematite (more than 50 wt.%), and goethite. On the top of FS, brown and ochreous goethite cement is commonly found filling cavities. Ochreous goethite together with kaolinite and gibbsite may cause the aspect of clay (fig. 5D). This sub horizon may also be referred as “chemical canga”.

The iron-crust on the top of the profile is coarse-grained (fig. 5E), stratified and highly porous. It is composed of grained to massive hematite, with brown and ochreous goethite cement (fig. 6K-L). This horizon is also called at the mine as “structural canga”, which may reach the depth of 30 m (fig. 3).

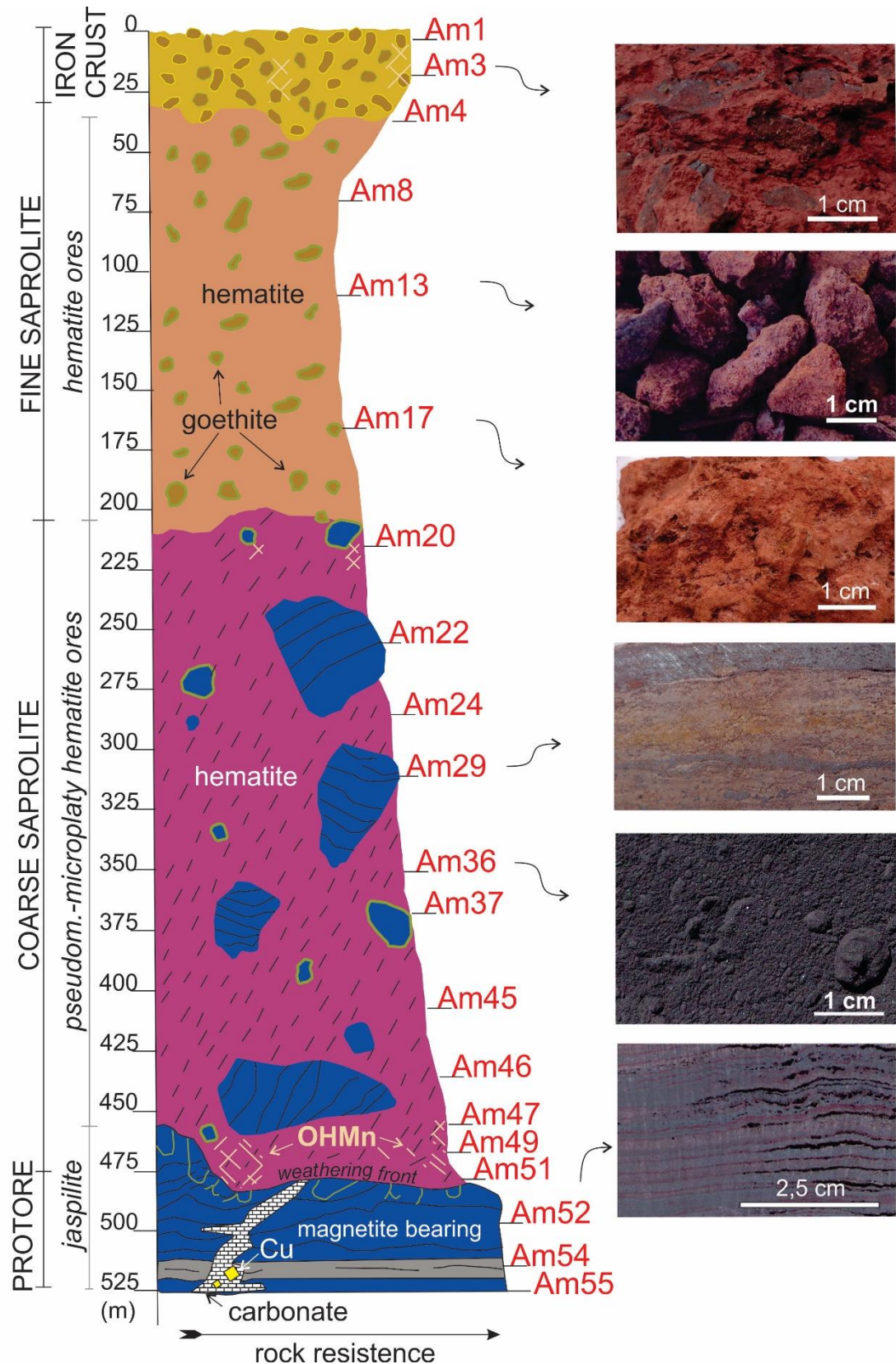


Figure 4- Simplified weathering profile and sample`s (20) location of the S11D mine, Carajás.

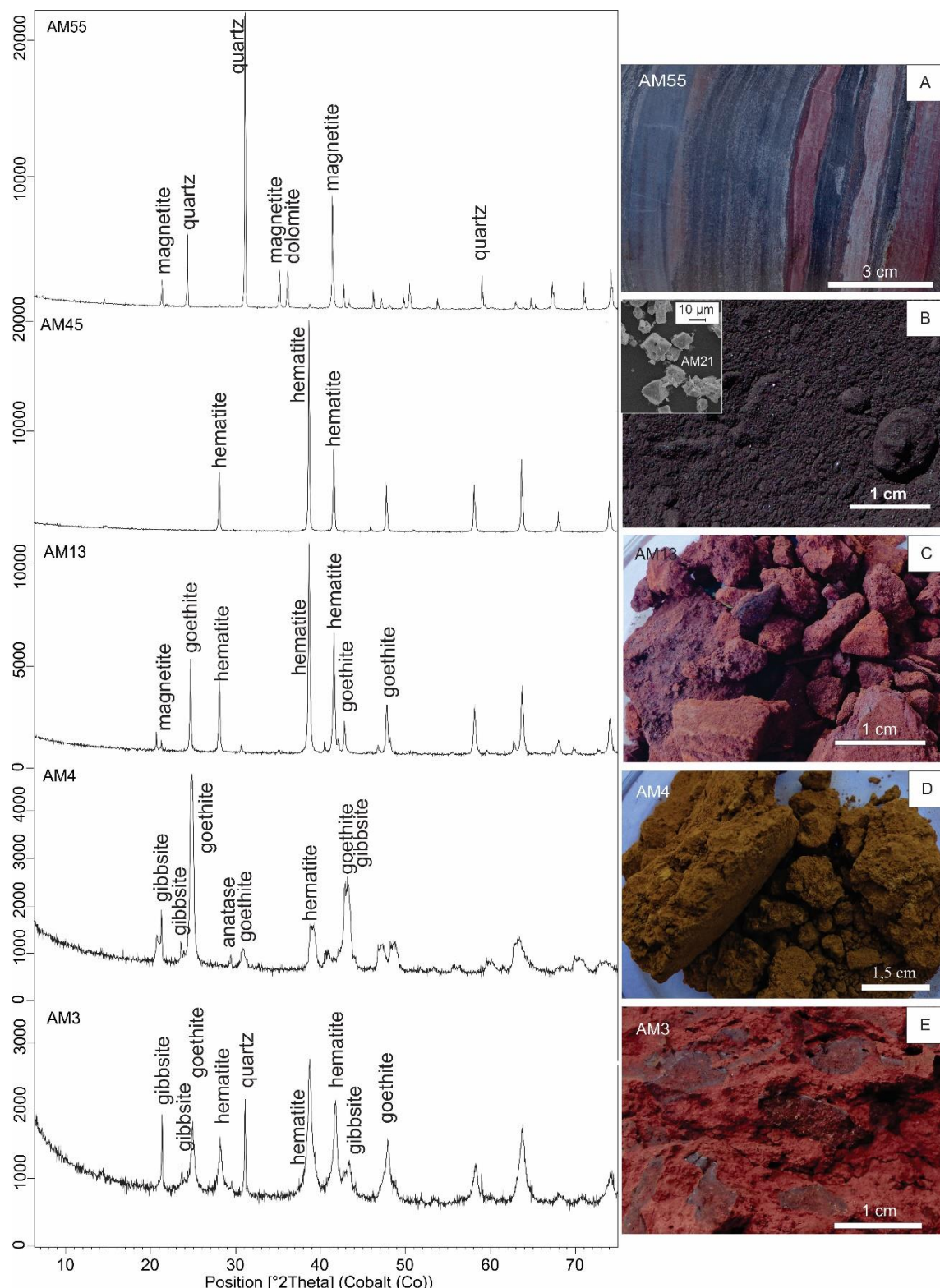


Figure 5- Mineralogy identified by XRD on the S11D samples. A) Jaspilite, black bands composed of hematite and magnetite, and light bands of jasper or chert; B) soft hematite, main composition is hematite (SEM micrography); C) hematite ore; D) ochreous goethite, probably aluminum-bearing; E) brown goethite, iron crust.

MICROTEXTURES TEXTURES RELATED TO THE IRON ORES

In the opaque and black bands of jaspilite, occur 90% of magnetite euhedral crystals (*mt*) and around 10% of primary-microplaty hematite (*mpl*). The primary structure of the jaspilite, as well as the parallel-banding, and the low porosity (fig. 6A) is preserved on the magnetite-bearing (fig. 4). Towards the top of the magnetite-bearing, the opaque bands were partially turned into pseudomorph hematite after magnetite (*psh*). The pseudomorphic substitution has occurred from the edges of the magnetite crystals toward its centers (fig. 6D-H).

There is an increase of the porosity from the protore into the saprolite in at least 50% of the volume. The porosity occurs between the crystals of hematite (interparticle) or inside of the pseudomorphic crystals (intraparticle). The interparticle porosity occurs as spherical to elongated centimeter long cavities (fig. 6F), which are most filled with different generations of goethite (fig. 6G-L). The intraparticle porosity is showed on the sharp or wave edges (fig. 6H), as well as ghost-crystals, where just the borders are preserved (fig. 6L).

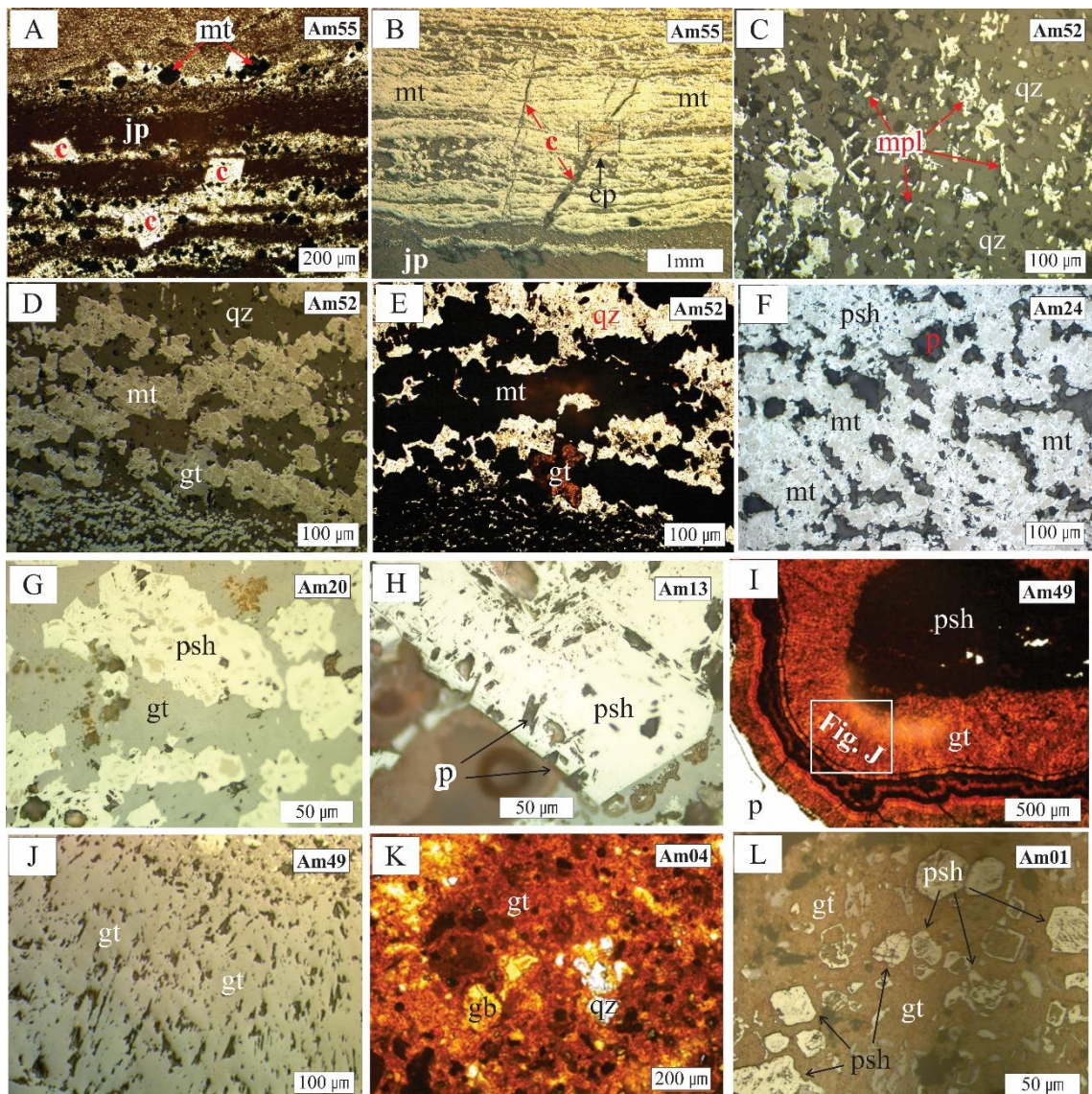


Figure 6- Mineralogy of the lateritic profile on the S11D samples. A) magnetite (mt), jasper (jp), and carbonate (c); B) light bands of magnetite, and dark bands of jasper; cross vein of chalcopyrite (Cp); C-F) leached BIF; C) microplaty hematite (mpl), magnetite (mt), and quartz (qz); D-H) magnetite and pseudomorphemic hematite after magnetite (psh); I) hematite with acicular radial brown goethite cement; J) detail of fig. I, acicular radial brown goethite; K-L) ochreous goethite and gibbsite (gb) in the crust. Photomicrographs under plane polarized light (A, E, I, K) and reflected light (B-L); micropores (p) are black.

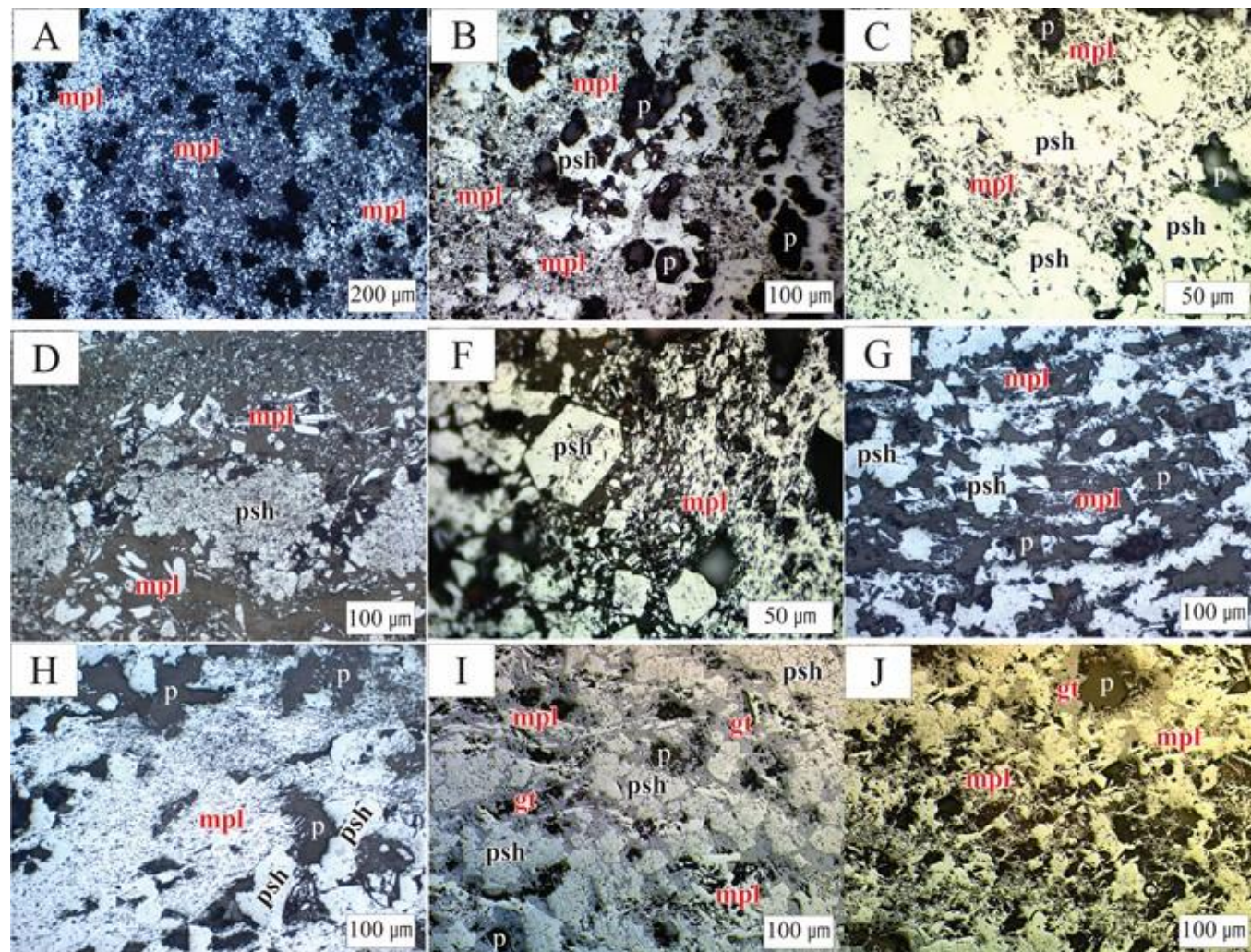


Figure 7- Hematite ore. A-J) Pseudomorphic hematite after magnetite (psh); microplaty hematite (mpl); goethite (gt) cement. Photomicrographs of typical primary ore textures under reflected light.

WHOLE-ROCK CHEMISTRY

MAJOR AND TRACE ELEMENTS

The twenty samples of S11D display a limited range of abundances for most major elements (table 2). This is well shown by the box and whisker plot (fig. 8), where the sum of Fe_2O_3 and SiO_2 make up to 70 % of the whole-rock chemistry for the majority of the samples (table 2). The total iron content is scattered at the intervals of 42.55-97.62 wt.% Fe_2O_3 (with median of 69 wt.%) (fig. 8). The content of SiO_2 in the whole profile raises from 0.1 to 56.17 wt.% (fig. 8). Indeed, SiO_2 and Fe_2O_3 concentrations are strongly negative correlated (fig. 10A). Only three components exhibit content more than 10% in isolate samples: Al_2O_3 (up to 16.24%), MnO (up to 23.7%) and the lost-on ignition (LOI, up to 14.35%). More than 75% of the samples show less than 1.0 wt.% Al_2O_3 (fig. 8).

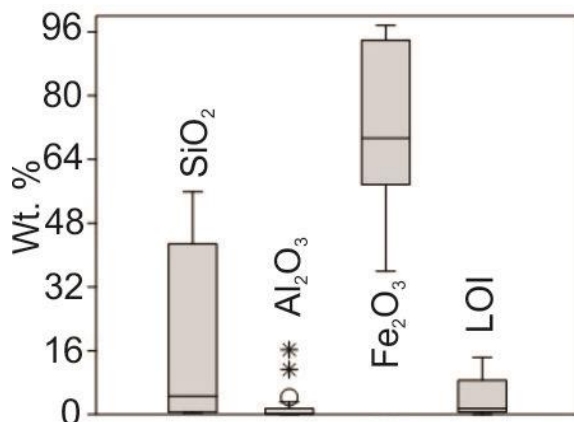


Figure 8- Box and whisker plot for the four major components of the 20 samples from S11D mine, Carajás. The full horizontal line is the median.

The content of TiO_2 and P_2O_5 on the protore and coarse saprolite occur in lower concentration (<0.02 ppm) (table 2). On the other side, the samples of fine saprolite and crust, when compared with the average of the upper continental crust (UCC, fig. 11), exhibit the maximum factor of enrichment of 2.25 for TiO_2 (0.1 to 1.45 wt.%) and 11.2 for P_2O_5 (0.1 to 1.68 wt.%). Whereas, Al_2O_3 exhibits a good positive correlation ($r = 0.85$) within the P_2O_5 (fig. 10B) and ($r = 0.99$) the TiO_2 (fig. 10C).

The alkali and alkali earth metals content ranges under 1.0 % of concentration in most of the samples (table 2). Although, concentrations > 1% can be found on the bottom of the profile where the amount of MgO ranges from 0.05 to 4.62 wt.%, CaO from 0.08 to 1.86 wt.%, and K_2O from 0.01 to 1.18 wt.%. Just MgO shows enrichment factor higher than 1 (table 2). MgO and CaO have negative correlation within each other, and their content are associated with the carbonates found in the BIFs and the mafic-carbonate

rock. MnO and K₂O show positive correlation ($r = 0.95$) locally (fig. 10D), mainly related to manganese oxides, such as cryptomelane and hollandite. The highest MnO content has been found at the bottom of the coarse saprolite, where it reached 24.19% MnO (median 0.6 wt.%) and 1.2% K₂O (median 0.5 wt.%).

The content of the investigated trace elements is variable along the horizons (fig. 9). In general, there are two groups of transition metals, which exhibit an enrichment factor >1.0 , either on the bottom or on the top of the profile, when compared with the UCC (table 2). The elements Co, Ni, Cu, Zn, Y, and Cd are largely concentrated on the protore and coarse saprolite horizons, while the elements Sc, V, Cr, Zr, Nb, Mo, Hf, Ta, W, and Hg are concentrated on the fine saprolite and on the crust, as well as the actinoids Th and U (fig. 9, 11B). Most of the transition metals display a positive correlation within Al₂O₃-TiO₂-P₂O₅, and between each other, as showed for Hf x Zr (fig. 10E) and Zr x TiO₂ (fig. 10F).

Other elements which are concentrated on the bottom of the coarse saprolite (AM49B) are Be, Sr, Ba, As, Ta (fig. 11A). When compared with the BIF average in Carajás, also Ba shows high concentration (fig. 12A) in this sample. The nonmetals (C, S, F and Cl) are concentrated on the mafic-carbonate rock, exceeding the values of concentration for the UCC with maximum factor of enrichment in up to 3 times (table 2). Ga, In, Pb, Sn, Bi, and Se exhibit higher concentration on the top of the profile (table 2). Those pos-transition metals have a positive correlation within Al₂O₃-TiO₂-P₂O₅ (fig. 9). Otherwise, Ga, Pb, Bi, Co, Ni, and Zn display an enrichment factor less than 1.0 on the fine saprolite and the crust (fig. 12B).

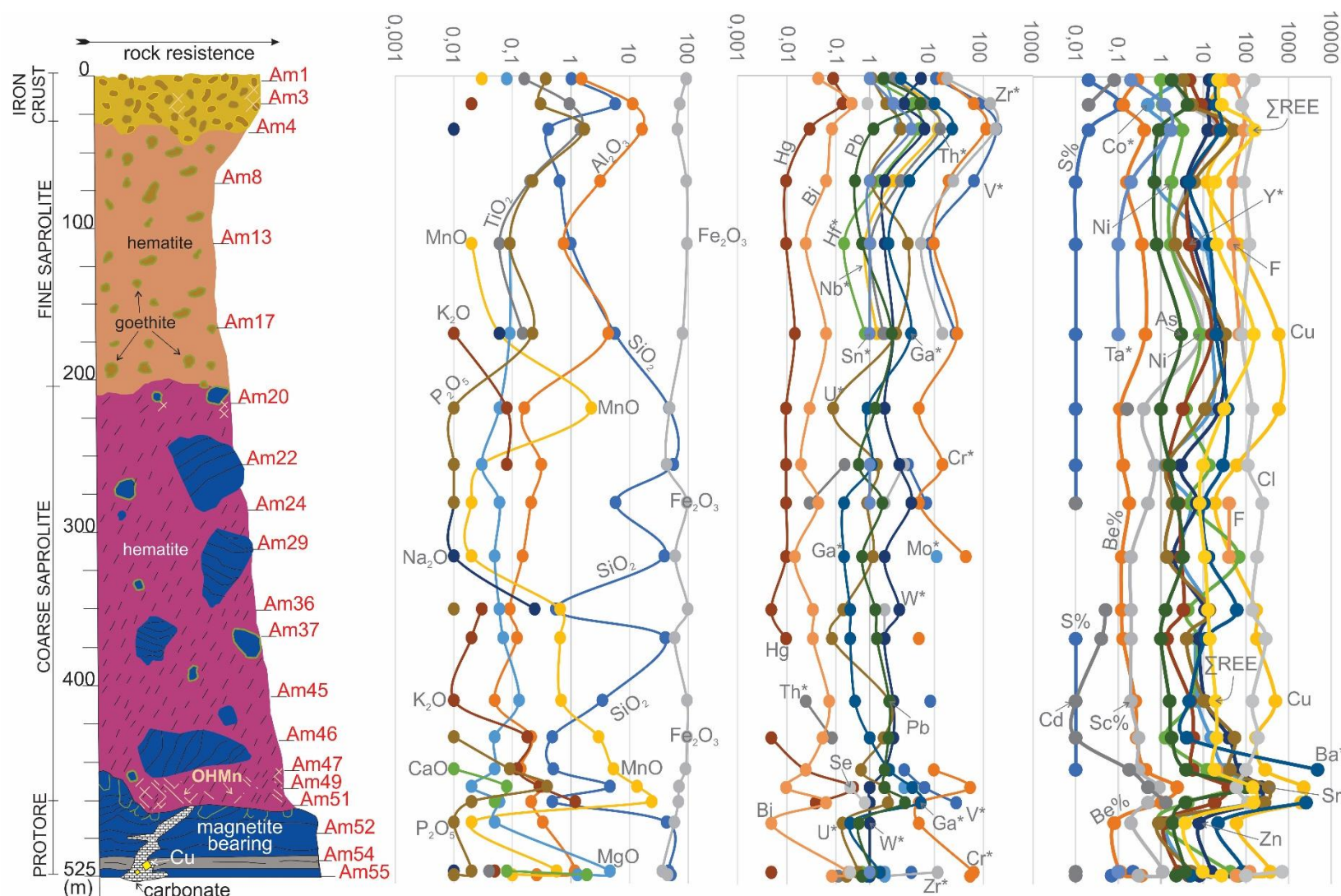


Figure 9- Chemostratigraphy of major and trace elements for 20 samples of S11D deposit. Noncontinuous lines are values under the detection limit.

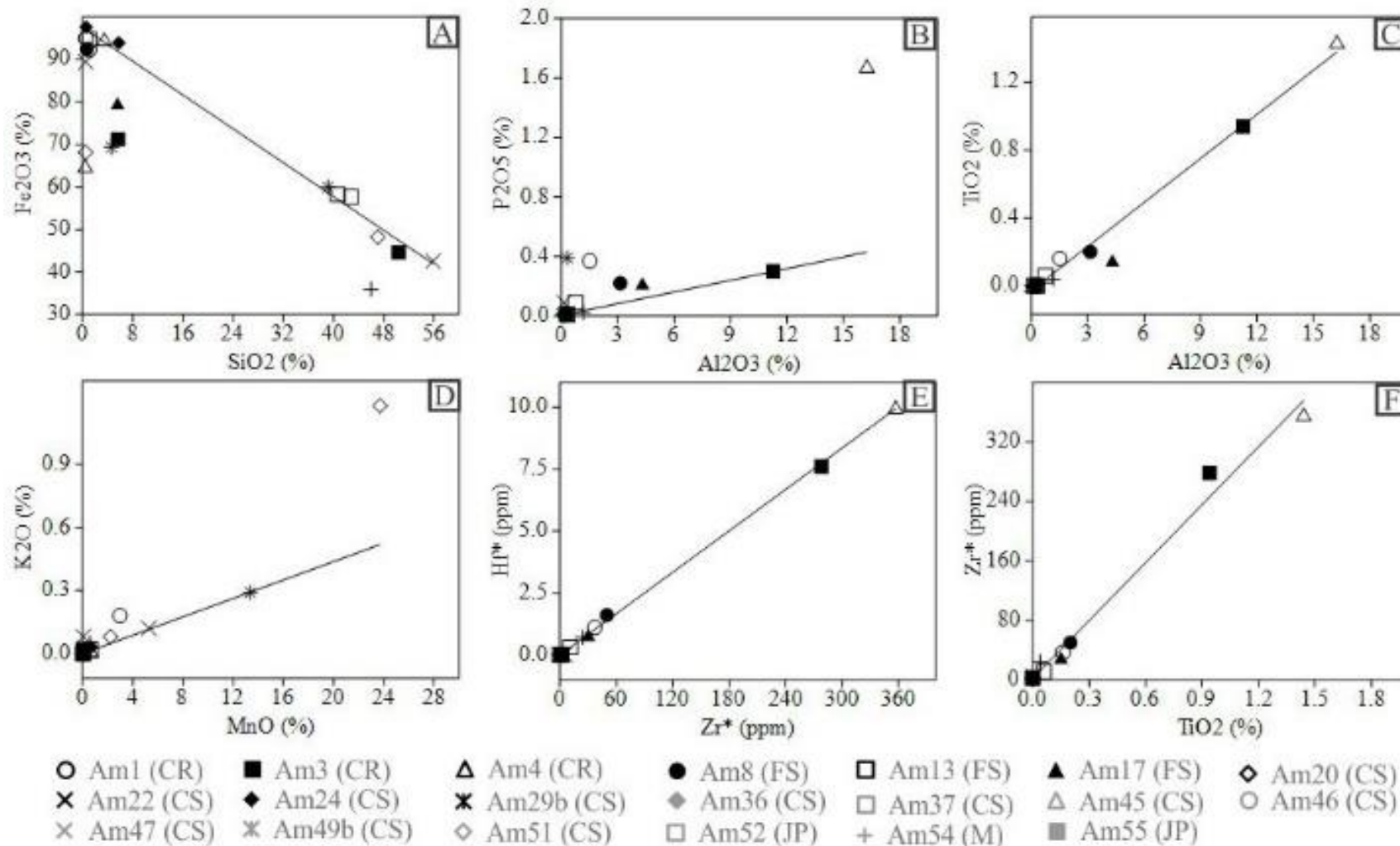


Figure 10- Linear model bivariate of elements correlation of the S11D samples: A) Fe₂O₃ x SiO₂; B) P₂O₅ x Al₂O₃; C) TiO₂ x Al₂O₃; D) K₂O x MnO; E) Hf x Zr; F) Zr x TiO₂. Horizons: CR – crust, FS – fine saprolite, CS – coarse saprolite, JP – jaspilite, M – mafic rock.

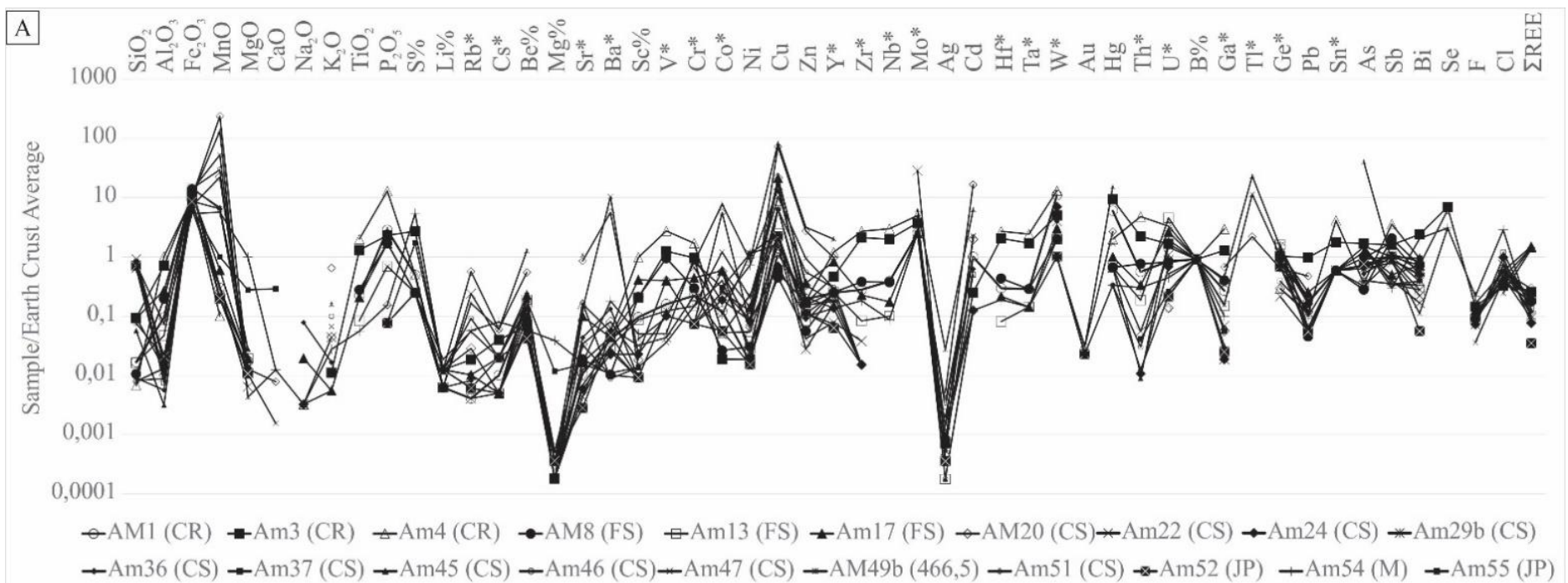


Figure 11- Chemical composition of the S11D samples normalized to the average values of the upper continental crust of the Earth after Rudnick & Gao (2003). A) Samples. CR – crust; FS – fine saprolite; CS – coarse saprolite; JP – jaspilite; M – mafic rock.

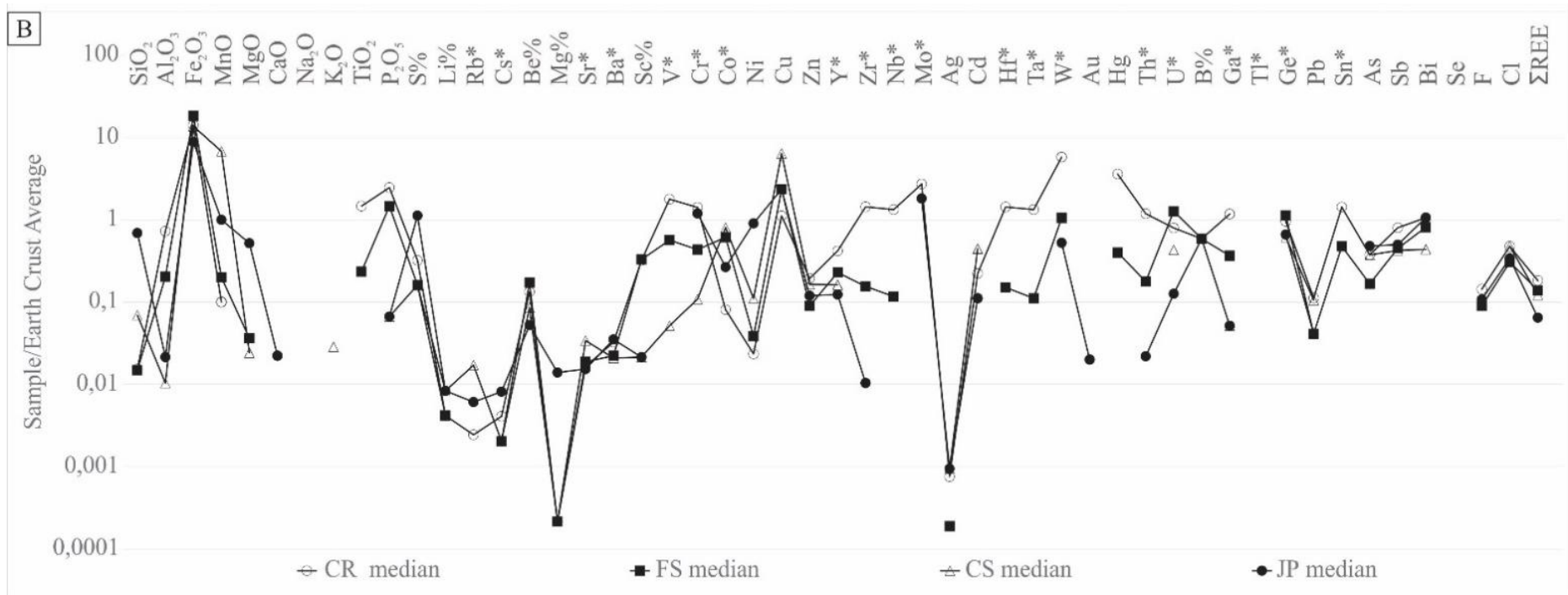


Figure 11- (cont.) Chemical composition of the S11D samples normalized to the average values of the upper continental crust of the Earth after Rudnick & Gao (2003). B) Median of samples in each horizon. CR – crust; FS – fine saprolite; CS – coarse saprolite; JP – jaspilite; M – mafic rock.

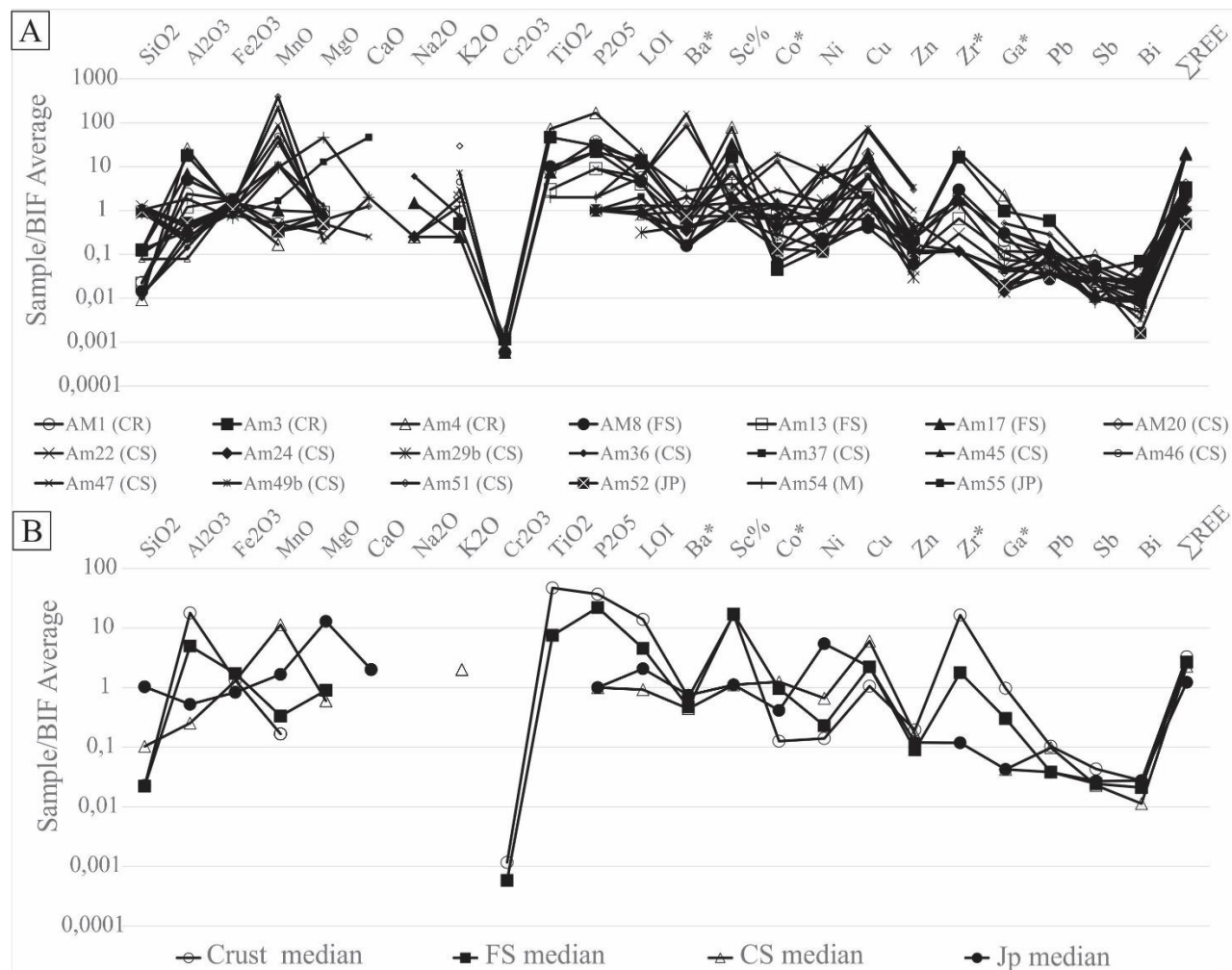


Figure 12- Chemical composition of the S11D samples normalized to the Carajás BIF average composition. Carajás BIF average composition after Macambira & Schrank (2002), Macambira (2003). A) Samples; B) Median of samples in each horizon. CR – crust; FS – fine saprolite; CS – coarse saprolite; JP – jaspilite; M – mafic rock.

Chondrite-normalized REE trends of these rocks are light rare earth element- (LREE) enriched (>1) and heavy rare earth element- (HREE) depleted (<1), with pronounced positive Eu- (median = 1.31) and negative Ce anomalies (median = 0.57) (table 2). Light depletion of Eu can be found in samples 3, 4, 54 and 55, while the sample 13 shows enrichment of Ce (fig. 13A). The lanthanoids display higher concentration of LREE on the coarse saprolite, while the HREE are more concentrated on the crust (fig. 13B). The largest Eu anomalies are in the saprolite samples, with a maximum of 3.07 (table 2).

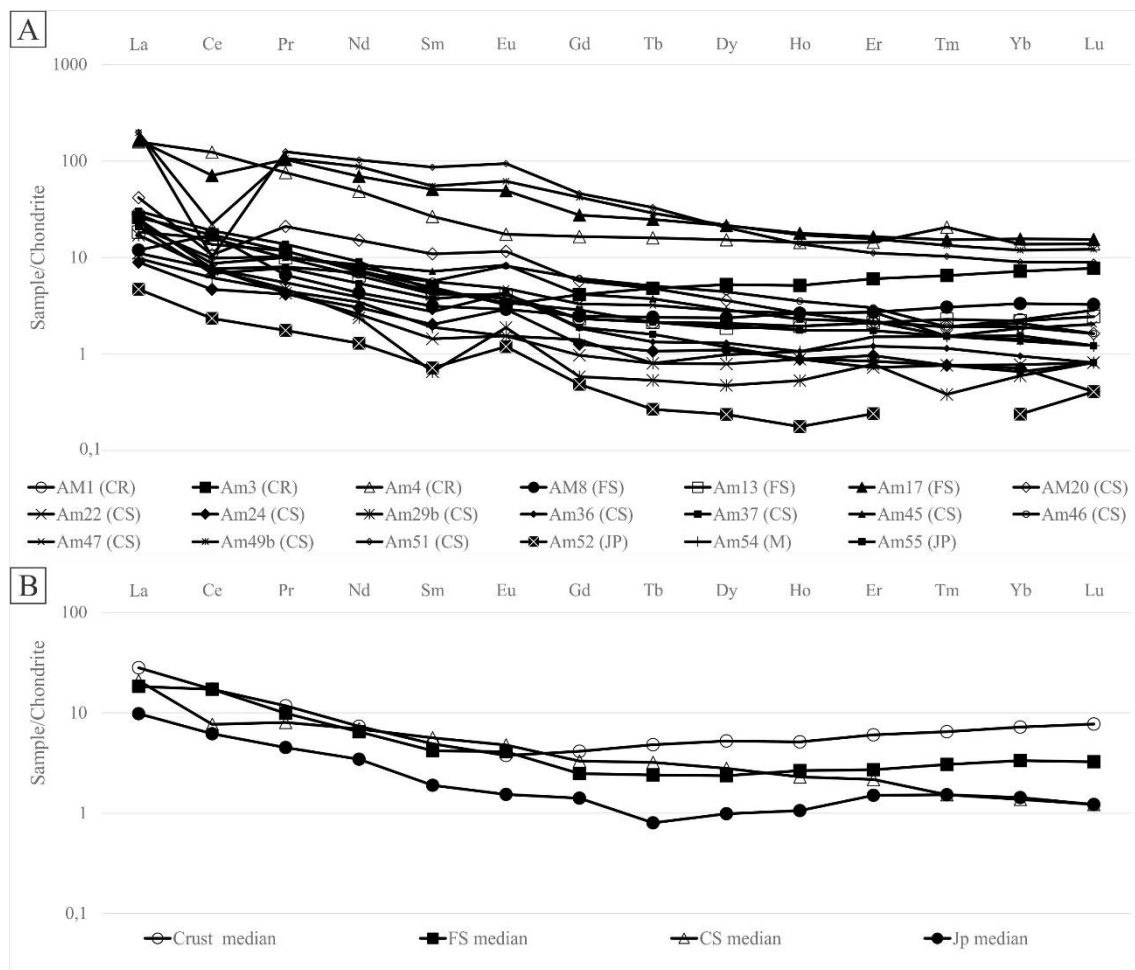


Figure 13- Rare Earth Elements distribution normalized to chondrites after Barrat *et al.* (2012) of the S11D samples. A) Samples; B) Median of samples in each horizon. CR – crust; FS – fine saprolite; CS – coarse saprolite; JP – jaspilite; M – mafic rock.

Table 2- Whole-rock chemistry of the 20 samples of SSDFD663 dill hole, at S11D deposit, Carajás Province. The major components are showed in oxides (wt. %) and trace elements in ppm. The numbers in parenthesis indicate the depth in meters of the sample. Average composition of the upper continental crust (UCC) after Rudnick & Gao (2003), (CH) Chondrites after Barrat *et al.* (2012) and BIF average of the Carajás Formation after Macambira & Schrank (2002), Macambira (2003). Unit (UNT), detection limit (DL), LOI – loss on ignition. Gold determinations by this method is semi-quantitative due to the small sample weight used. *Elements determined by Li borate fusion ICP-MS, used in the graphics in figures 9 to 13. Cs < 0.05

COMP.	UNT	DL	Crust			Fine saprolite				Coarse saprolite						
			AM1	AM3 (2)	AM4 (18.3)	AM8 (35)	AM13 (69)	AM17 (110)	AM20 (169)	AM22 (218)	AM24 (255)	AM29 (280)	AM36 (315.3)	AM37 (350)	AM45 (369)	AM45 (410)
SiO ₂	%	0.01	1.02	5.66	0.41	0.64	0.99	5.56	47.08	55.88	5.76	39.11	0.55	40.64	3.44	
Al ₂ O ₃	%	0.01	1.51	11.26	16.24	3.13	0.75	4.31	0.16	0.31	0.21	0.15	0.09	0.12	0.05	
Fe ₂ O ₃	%	0.01	92.23	71.23	64.95	92.47	94.78	79.7	48.22	42.55	93.92	59.96	97.62	58.26	94.76	
MnO	%	0.01	0.03	<0.01	0.01	<0.01	0.02	0.06	2.22	0.03	0.02	0.02	0.65	0.65	0.68	
MgO	%	0.01	0.08	<0.01	<0.01	<0.01	0.09	0.09	0.06	0.03	0.06	0.05	0.06	0.07	0.13	
CaO	%	0.01	<0.01	<0.01	<0.01	<0.01	<0.01	<0.01	<0.01	<0.01	<0.01	<0.01	<0.01	<0.01	<0.01	
Na ₂ O	%	0.01	<0.01	<0.01	0.01	<0.01	<0.01	0.06	<0.01	0.01	0.01	0.01	0.24	<0.01	0.01	
K ₂ O	%	0.01	<0.01	0.02	<0.01	<0.01	<0.01	0.01	0.08	0.08	<0.01	<0.01	0.03	0.02	0.01	
BaO	%	0.01	<0.01	<0.01	<0.01	<0.01	<0.01	<0.01	<0.01	<0.01	<0.01	<0.01	<0.01	<0.01	<0.01	
Cr ₂ O ₃	%	0.01	<0.01	0.02	0.03	0.01	<0.01	0.01	<0.01	<0.01	0.01	0.02	<0.01	<0.01	<0.01	
TiO ₂	%	0.01	0.16	0.94	1.44	0.2	0.06	0.15	<0.01	<0.01	<0.01	<0.01	<0.01	<0.01	<0.01	
P ₂ O ₅	%	0.01	0.37	0.3	1.68	0.22	0.09	0.22	0.01	0.01	0.01	<0.01	0.01	<0.01	<0.01	
SO ₃	%	0.01	0.42	0.29	0.39	0.03	0.01	0.03	0.02	<0.01	0.04	<0.01	0.03	0.02	<0.01	
SrO	%	0.01	<0.01	<0.01	0.01	0.01	<0.01	0.01	<0.01	<0.01	0.01	<0.01	0.01	0.01	<0.01	
LOI	%	0.01	4.05	10.13	14.35	3.31	2.92	8.75	0.95	0.59	0.66	0.23	0.67	0.52	0.61	
Total	%	0.01	99.92	99.94	99.65	100.1	99.73	99.12	99.08	99.5	100.8	99.58	100.05	100.45	99.8	
C	%	0.01	0.21	0.8	0.14	0.05	0.07	0.08	0.07	0.06	0.08	0.04	0.05	0.05	0.06	
S	%	0.01	0.02	0.11	0.02	0.01	0.01	0.01	0.01	0.01	0.01	<0.01	<0.01	0.01	0.01	
S	%	0.01	0.01	0.08	0.01	<0.01	<0.01	<0.01	<0.01	<0.01	<0.01	<0.01	<0.01	<0.01	<0.01	
F	ppm	20	50	80	90	50	50	70	<20	<20	40	40	<20	<20	<20	
Cl	ppm	50	150	80	140	90	120	80	140	110	240	180	140	290	140	
Li	ppm	0.1	0.1	0.2	0.1	0.1	0.1	0.2	0.2	0.1	0.2	0.1	0.1	0.2	0.2	
Na	%	0.01	0.01	<0.01	<0.01	<0.01	<0.01	<0.01	0.01	<0.01	0.01	<0.01	<0.01	<0.01	<0.01	
K	%	0.01	<0.01	<0.01	<0.01	<0.01	<0.01	<0.01	0.07	0.01	<0.01	<0.01	0.01	0.02	0.01	
Rb	ppm	0.1	0.1	0.2	<0.1	<0.1	0.1	0.2	1.2	2.1	0.1	0.3	0.4	0.3		
Rb*	ppm	0.2	0.2	0.9	<0.2	<0.2	<0.2	0.5	1.4	11.8	0.3	0.2	0.4	0.5	0.3	
Cs	ppm	0.05	<0.05	<0.05	<0.05	<0.05	<0.05	<0.05	<0.05	<0.05	<0.05	<0.05	<0.05	<0.05	<0.05	
Cs*	ppm	0.01	0.02	0.08	<0.01	<0.01	0.01	0.01	0.01	0.08	0.01	0.01	<0.01	0.01	0.01	
Be	ppm	0.05	0.28	0.13	0.41	0.16	0.36	0.43	0.11	0.13	0.18	0.12	0.12	0.13	0.25	
Mg	%	0.01	0.02	0.01	<0.01	<0.01	0.01	0.01	0.01	0.01	0.01	0.01	0.02	0.01	0.03	
Ca	%	0.01	0.01	0.02	<0.01	<0.01	0.01	0.01	0.01	0.01	0.01	0.01	<0.01	0.01		
Sr	ppm	0.2	0.5	0.5	10.5	0.8	0.5	0.7	9.8	0.8	1	0.8	8.6	3.3	8.7	
Sr*	ppm	0.1	3.4	5.3	51.3	6	2.2	31.8	10.9	1.4	1.9	1.4	13.9	4	10.5	
Ba	ppm	10	20	10	10	<10	10	10	40	20	10	10	60	10	<10	
Ba*	ppm	0.5	18.5	20.4	25.1	4.7	14	20	36.9	28.7	10.3	13.1	60.5	11.5		
B	ppm	10	10	10	10	10	10	10	<10	<10	<10	<10	10	<10	10	
Ge	ppm	0.05	1.91	1.34	0.38	1.39	2.11	1.59	0.38	0.28	1.29	1.96	0.85	0.51	0.86	
As	ppm	0.1	1.8	4.2	0.9	0.7	0.8	3	1	1.6	2.4	3.3	1.3	1	1.6	
Sb	ppm	0.05	0.18	0.32	0.71	0.41	0.18	0.1	0.07	0.16	0.35	0.08	0.2	0.07	0.22	
Te	ppm	0.01	0.03	1.1	0.28	0.04	0.04	0.03	0.03	0.01	<0.01	0.02	0.03	0.03	0.02	
Sc	ppm	0.1	2.1	4.5	21.4	4.6	1.9	9	0.4	0.7	0.5	0.2	0.2	0.2		
Ti	%	0.005	0.029	0.1	0.101	0.033	0.014	0.023	<0.005	<0.005	<0.005	<0.005	<0.005	<0.005	<0.005	
V	ppm	1	14	130	193	82	12	44	3	4	12	2	1	7		
V*	ppm	5	22	173	378	131	17	55	<5	6	14	<5	<5	<5		
Cr	ppm	1	14	97	124	16	13	39	1	29	7	152	<1	9	<1	
Cr*	ppm	10	30	130	230	40	20	60	10	30	10	90	<10	10	<10	
Mn	ppm	5	143	<5	<5	21	69	425	17300	249	176	116	4250	4830	5370	
Fe	%	0.01	28.2	43	24	19.05	22.9	27.7	12.05	13.15	23.2	17.25	23.1	12.85	21.4	
Co	ppm	0.1	1.3	0.2	0.7	0.3	3.6	9	14.3	1	2.4	2	14.1	5.4	5.7	
Co*	ppm	0.5	3.2	0.5	1.4	0.7	10.6	15.6	15.2	1.3	5	2.9	13.9	6.8	7.4	
Ni	ppm	0.2	1	1.1	3.2	1.8	1.7	8.3	3.9	13.4	4.9	66.7	4.3	7.2	5.2	
Cu	ppm	0.2	31.3	14.7	42.5	12.1	66.2	578	590	60.3	18.7	45	172.5	179.5		
Zn	ppm	2	14	12	13	4	6	26	24	3	7	2	11	8	11	
Y	ppm	0.05	1.07	0.27	3.51	0.81	1.75	7.48	3.08	0.5	1.03	0.62	2.27	1.16	3.84	
Y*	ppm	0.5	4.7	8.8	22.8	4.8	4.8	15.9	3.3	1.5	2.6	3	3.4	1.4	4.9	
Zr	ppm	0.5	7	31.6	4.6	4.5	3.6	4.1	<0.5	0.8	<0.5	<0.5	<0.5	<0.5		
Zr*	ppm	2	37	278	357	50	11	30	<2	5	2	<2	2	2	<2	
Nb	ppm	0.05	0.45	2.22	0.43	0.35	0.13	0.11	<0.05	0.09	0.05	0.07	0.06	<0.05	0.05	
Nb*	ppm	0.2	3.1	16	23.9	3	0.8	1.4	<0.2	<0.2	<0.2	<0.2	<0.2	<0.2		
Mo	ppm	0.05	0.6	1.92	0.87	0.22	0.23	0.69	0.36	0.77	0.37	15.65	0.27	0.31	0.25	
Mo*	ppm	2	2	3	4	<2	<2	2	<2	<2	<2	23	<2	<2		
Ag	ppm	0.01	0.18	0.04	0.02	<0.01	0.01	0.02	0.08	0.06	0.05	0.03	0.03	0.11	0.01	
Cd	ppm	0.01	0.08	0.02	<0.01	<0.01	<0.01	<0.01	0.16	<0.01	0.01	<0.01	0.05	0.04	0.01	
Hf	ppm	0.02	0.19	0.93	0.13	0.13	0.11	0.15	<0.02	0.02	<0.02	<0.02	<0.02	<0.02		
Hf*	ppm	0.2	1.1	7.6	10	1.6	0.3	0.8	<0.2	<0.2	<0.2	<0.2	<0.2	<0.2		
Ta	ppm	0.01	0.01	0.03	0.02	0.02	<0.01	<0.01	<0.01	<0.01	<0.01	<0.01	<0.01	<0.01		
Ta*	ppm	0.1	0.2	1.2	1.7	0.2	0.1	0.1	<0.1	<0.1	<0.1	<0.1	<0.1	<0.1		
W	ppm	0.05	2.82	0.45	0.51	0.16	0.18	0.55	1.08	0.23	2.37	0.28	1.02	0.55	0.27	
W*	ppm	1	11	5	13	2	2	3	2	4	7	2	4	2	3	
Re	ppm	0.001	<0.001	0.001	0.001	<0.001	<0.001	0.001	<0.001	0.001	0.001	0.001	<0.001	<0.001	<0.001	
Au	ppm	0.02	<0.02	<0.02	<0.02	<0.02	<0.02	<0.02	<0.02	<0.02	<0.02	<0.02	<0.02	<0.02		
Hg	ppm	0.01	0.18	0.28	0.06	0.02	0.02	0.03	0.02	0.02	0.02	0.02	0.01	0.02	<0.01	
Th	ppm	0.2	1.5	8.7	6.3	0.9	0.3	0.8	<0.2	0.3	<0.2	<0.2	<0.2	<0.2		
Th*	ppm	0.05	3.14	12.45	26.8	4.28	1.04	1.87	<0.05	0.31	0.06	<0.05	0.07	<0.05		

U	ppm	0.05	0.29	0.93	1.86	0.29	2.52	2.19	0.14	0.93	0.56	0.86	0.16	0.13	1.3
U*	ppm	0.05	1.1	2.15	4.3	1.06	5.93	3.44	0.18	1.41	0.89	1.16	0.29	0.17	2.51
Al	%	0.01	0.58	3.61	3.78	1.19	0.29	0.74	0.07	0.06	0.05	0.08	0.04	0.05	0.03
Ga	ppm	0.05	2.92	16.15	26.1	3.01	1.45	3.91	0.8	0.57	0.14	0.09	0.19	0.24	0.34
Ga*	ppm	0.1	4.3	20.6	47.1	6.4	2.4	6.9	0.9	1.1	0.3	0.3	0.4	0.4	0.5
In	ppm	0.005	0.026	0.08	0.19	0.034	0.008	0.026	<0.005	0.008	0.005	<0.005	0.011	0.006	0.015
Tl	ppm	0.02	<0.02	<0.02	<0.02	<0.02	<0.02	0.03	0.02	<0.02	<0.02	<0.02	<0.02	<0.02	<0.02
Tl*	ppm	0.5	<0.5	<0.5	<0.5	<0.5	<0.5	<0.5	<0.5	<0.5	<0.5	<0.5	<0.5	<0.5	<0.5
Pb	ppm	0.2	1.9	10.7	1.2	0.5	0.7	2.8	1.3	0.6	1.8	0.7	1.3	1.4	2.5
Sn	ppm	0.2	0.3	1.7	3.6	0.7	0.2	0.2	<0.2	0.5	<0.2	0.2	<0.2	<0.2	<0.2
Sn*	ppm	1	1	3	7	1	1	1	<1	1	1	<1	<1	<1	<1
P	ppm	10	1120	940	3650	630	270	610	20	30	20	10	10	10	10
Bi	ppm	0.01	0.09	0.43	0.17	0.13	0.05	0.13	0.06	0.04	0.09	0.03	0.07	0.07	0.15
Se	ppm	0.2	<0.2	0.9	<0.2	<0.2	<0.2	<0.2	<0.2	<0.2	<0.2	<0.2	<0.2	<0.2	<0.2
La	ppm	0.2	0.7	0.7	0.3	0.2	1	4.1	8.3	0.6	0.8	1.8	2.9	2.9	2.6
La*	ppm	0.5	6.6	6.1	37.1	2.8	4.3	38.5	9.8	2.6	2.1	4	4.9	5.4	
Ce	ppm	0.02	1.14	1.37	0.76	0.84	1.33	6.65	5.18	2.93	1.98	2.68	3.39	2.44	2.73
Ce*	ppm	0.5	8.2	10.3	74.1	10.3	9.5	42.6	6.4	4.6	2.8	4.5	4.6	4.1	5.2
Pr*	ppm	0.03	1.07	1.06	6.9	0.6	0.9	9.44	1.91	0.39	0.38	0.43	0.5	0.71	0.91
Nd*	ppm	0.1	3.3	3.4	22.5	2	3	32.2	7	1.2	1.4	1.1	1.8	2.5	3.9
Sm*	ppm	0.03	0.67	0.75	4.07	0.48	0.64	7.79	1.67	0.22	0.31	0.1	0.42	0.57	1.1
Eu*	ppm	0.1	0.22	0.19	1.02	0.17	0.24	2.89	0.68	0.09	0.17	0.11	0.25	0.25	0.49
Gd*	ppm	0.05	0.48	0.85	3.4	0.51	0.48	5.67	1.17	0.2	0.26	0.12	0.38	0.39	0.86
Tb*	ppm	0.01	0.08	0.18	0.6	0.09	0.08	0.93	0.18	0.03	0.04	0.02	0.05	0.06	0.14
Dy*	ppm	0.05	0.53	1.33	3.88	0.6	0.47	5.44	0.91	0.2	0.28	0.12	0.33	0.3	0.73
Ho*	ppm	0.01	0.11	0.29	0.81	0.15	0.11	1.01	0.15	0.05	0.05	0.03	0.06	0.05	0.13
Er*	ppm	0.03	0.35	1	2.38	0.45	0.35	2.73	0.36	0.12	0.16	0.13	0.2	0.14	0.36
Tm*	ppm	0.01	0.05	0.17	0.54	0.08	0.06	0.4	0.05	0.02	0.02	0.01	0.03	0.02	0.04
Yb*	ppm	0.03	0.38	1.21	2.31	0.56	0.37	2.62	0.32	0.13	0.12	0.1	0.16	0.11	0.23
Lu*	ppm	0.01	0.07	0.19	0.34	0.08	0.06	0.38	0.04	0.02	0.01	0.02	0.02	0.02	0.03
Eu/Eu*	ppm		1.19	0.73	0.84	1.05	1.32	1.33	1.49	1.31	1.83	3.07	1.91	1.62	1.54
Ce/Ce*	ppm		0.57	0.77	0.92	1.65	1.00	0.49	0.29	0.82	0.60	0.53	0.53	0.38	0.43
Σ REE			20.54	22.65	149.1	16.86	19.06	139.1	28.63	9.3	7.42	10.36	11.95	13.42	17.86
Σ HREE			1.57	4.37	10.86	2.01	1.5	13.51	2.01	0.57	0.68	0.43	0.85	0.7	1.66
Σ REE			22.11	27.02	160	18.87	20.56	152.6	30.64	9.87	8.1	10.79	12.8	14.12	19.52

Table 2- (Cont.)

COMP.	UNT	DL	Coarse Saprolite				Protore				UCC	CH	BIF	Factor Min./Max.
			AM46 (434)	AM47 (455)	AM49b (466.5)	AM51 (476.5)	AM52 (490)	AM54 (522)	AM55 (524.5)					
SiO ₂	%	0.01	0.48	0.5	4.61	0.48	42.82	45.99	50.39	66.6	44.6	0.01/0.84		
Al ₂ O ₃	%	0.01	0.21	0.14	0.32	0.21	0.33	1.16	0.26	15.4	0.63	0.00/1.05		
Fe ₂ O ₃	%	0.01	94.97	89.39	69.36	68.15	57.68	35.93	44.59	5.04	53.65	7.13/19.37		
MnO	%	0.01	2.96	5.28	13.35	23.7	0.02	0.57	0.1	0.10	0.06	0.10/237.00		
MgO	%	0.01	0.05	0.05	0.02	0.06	0.05	4.62	1.29	2.48	0.1	0.01/1.86		
CaO	%	0.01	<0.01	0.01	0.08	0.05	<0.01	0.08	1.86	3.59	0.04	0.00/0.52		
Na ₂ O	%	0.01	<0.01	<0.01	<0.01	<0.01	<0.01	<0.01	<0.01	3.27	0.04	0.00/0.07		
K ₂ O	%	0.01	0.18	0.12	0.29	1.18	<0.01	0.05	<0.01	2.80	0.04	0.00/0.42		
BaO	%	0.01	<0.01	0.52	1.32	0.29	<0.01	<0.01	<0.01			/		
Cr ₂ O ₃	%	0.01	<0.01	0.01	0.01	<0.01	<0.01	<0.01	<0.01			/		
TiO ₂	%	0.01	<0.01	<0.01	<0.01	<0.01	<0.01	0.04	<0.01	0.64	0.02	0.06/2.25		
P ₂ O ₅	%	0.01	0.01	0.09	0.39	0.02	0.01	0.02	0.01	0.15	0.01	0.07/11.20		
SO ₃	%	0.01	0.03	<0.01	0.04	0.03	0.02	0.52	0.2			/		
SrO	%	0.01	0.01	0.01	0.04	0.04	0.01	<0.01	0.01			/		
LOI	%	0.01	0.86	4.24	8.57	4.14	-0.13	11.4	1.51		0.73	/		
Total	%	0.01	100.05	100.85	99.86	100.5	100.85	100.55	100.25	100.05	-	0.99/1.01		
C	%	0.01	0.06	0.04	0.08	0.05	0.06	3.39	0.81			/		
S	%	0.01	0.01	0.01	<0.01	<0.01	<0.01	0.22	0.07	0.062		0.16/3.54		
S	%	0.01	<0.01	<0.01	<0.01	<0.01	<0.01	0.23	0.08	0.062		0.16/3.70		
F	ppm	20	<20	20	<20	<20	<20	120	60	557		0.04/0.22		
Cl	ppm	50	190	100	60	110	<50	700	100	294		0.20/2.38		
Li	ppm	0.1	0.2	0.3	0.1	0.2	0.2	0.2	0.2	24	1.44	0.00/0.01		
Na	%	0.01	<0.01	0.01	<0.01	<0.01	<0.01	<0.01	<0.01			/		
K	%	0.01	0.15	0.1	0.24	0.95	<0.01	0.01	0.01		0.055	/		
Rb	ppm	0.1	4.4	2.5	6.7	30.7	0.1	1.7	0.3	82	2.33	0.00/0.37		
Rb*	ppm	0.2	4.5	2.7	8.1	27.7	0.3	2.8	0.5	82	2.33	0.00/0.34		
Cs	ppm	0.05	<0.05	<0.05	0.06	<0.05	<0.05	0.1	<0.05	4.9	0.189	0.01/0.02		
Cs*	ppm	0.01	0.04	0.04	0.12	0.12	0.04	0.16	0.04	4.9	0.189	0.00/0.03		
Be	ppm	0.05	0.27	0.43	2.42	1.04	0.08	0.11	0.35	2.1	0.023	0.04/1.15		
Mg	%	0.01	0.02	0.01	<0.01	<0.01	0.02	2.15	0.65	46.7	9.42	0.00/0.05		
Ca	%	0.01	0.02	0.01	0.07	0.05	0.01	0.08	1.25		0.84	/		
Sr	ppm	0.2	51.9	38.2	304	277	0.6	0.4	4.4	320	7.73	0.00/0.95		
Sr*	ppm	0.1	53.7	41.7	345	273	0.9	5.2	4.9	320	7.74	0.00/1.08		
Ba	ppm	10	<10	4550	>10000	2540	20	80	10	628	2.46	29.73	0.02/7.25	
Ba*	ppm	0.5	4	4750	>10000	2560	22.1	82.1	5	628	2.46		0.01/7.56	
B	ppm	10	10	10	<10	<10	10	10	10		17		0.59/0.59	
Ge	ppm	0.05	1.09	1.35	1.93	0.84	0.9	1.23	0.93	1.4			0.20/1.51	
As	ppm	0.1	1.8	3.9	100.5	3.8	1.9	3.7	2.3	4.8			0.15/20.94	
Sb	ppm	0.05	0.22	0.07	0.17	0.2	0.2	0.06	0.2	0.4	7.43		0.15/1.78	
Te	ppm	0.01	<0.01	0.03	0.02	<0.01	0.02	0.07	0.03				/	
Sc														

Co	ppm	0.1	12.1	30.7	194.5	171.5	1	3.5	6.8	17.3	519	11.1	0.01/11.24
Co*	ppm	0.5	15.1	32.3	208	149.5	1.5	4.6	8.1	17.3	520		0.03/12.02
Ni	ppm	0.2	1.3	12.1	51.3	4.3	0.9	42.6	67.2	47	11300	7.85	0.02/1.43
Cu	ppm	0.2	172.5	278	2250	1955	59.8	373	66.1	28	127	29.79	0.43/80.4
Zn	ppm	2	40	68	228	197	8	15	8	67	303	66.58	0.03/3.40
Y	ppm	0.05	5.21	4.16	26.1	19.85	1.02	1.04	2.2	21		1.56	0.01/1.24
Y*	ppm	0.5	5.8	5.6	38	18.4	1.2	2.6	4.5	21		1.56	0.06/1.81
Zr	ppm	0.5	<0.5	<0.5	<0.5	<0.5	<0.5	4.1	0.6	193	3.52	16.89	0.00/0.16
Zr*	ppm	2	2	<2	<2	<2	<2	24	2	193	3.52	16.89	0.01/1.85
Nb	ppm	0.05	0.05	0.06	<0.05	<0.05	<0.05	0.05	0.11	12	0.289		0.00/0.19
Nb*	ppm	0.2	<0.2	<0.2	<0.2	<0.2	<0.2	0.7	<0.2	12	0.289		0.06/1.99
Mo	ppm	0.05	0.25	0.68	2.84	0.58	0.15	1.45	2.51	1.1			0.14/14.23
Mo*	ppm	2	<2	<2	5	<2	<2	2	2				1.82/20.91
Ag	ppm	0.01	0.01	0.04	1.54	0.29	0.02	0.08	0.05	53			0.00/0.03
Cd	ppm	0.01	0.01	0.18	0.5	1.32	<0.01	0.01	0.01	0.09			0.11/14.67
Hf	ppm	0.02	0.02	<0.02	0.03	0.02	0.03	0.15	0.05	5.3	0.107		0.00/0.18
Hf*	ppm	0.2	<0.2	<0.2	<0.2	<0.2	<0.2	0.7	<0.2	5.3	0.107		0.06/1.89
Ta	ppm	0.01	<0.01	<0.01	<0.01	<0.01	<0.01	<0.01	<0.01	0.9	0.015		0.01/0.03
Ta*	ppm	0.1	<0.1	<0.1	<0.1	<0.1	<0.1	0.1	<0.1	0.9	0.015		0.11/1.89
W	ppm	0.05	0.53	0.16	0.17	0.61	0.35	0.17	0.37	1.9	0.11		0.08/1.48
W*	ppm	1	3	2	1	1	1	1	1	1.9	0.11		0.53/6.84
Re	ppm	0.001	0.001	0.001	<0.001	<0.001	<0.001	0.002	<0.001	0.198			0.01/0.01
Au	ppm	0.02	<0.02	<0.02	0.04	0.04	0.03	0.03	0.03	1.5			0.02/0.03
Hg	ppm	0.01	0.01	0.05	0.46	0.08	<0.01	0.01	<0.01	0.05			0.20/9.20
Th	ppm	0.2	<0.2	<0.2	<0.2	<0.2	<0.2	0.7	0.2	10.5	0.028		0.02/0.83
Th*	ppm	0.05	0.17	<0.05	<0.05	<0.05	<0.05	1.69	0.23	10.5	0.028		0.00/2.55
U	ppm	0.05	1.16	0.36	1.4	1.95	0.19	0.19	0.26	2.7	0.008		0.05/0.93
U*	ppm	0.05	1.91	0.67	1.96	2.34	0.28	0.58	0.34	2.7	0.008		0.06/2.20
Al	%	0.01	0.12	0.09	0.11	0.1	0.16	0.52	0.11	0.79			/
Ga	ppm	0.05	1.3	1.26	1.51	2.77	0.25	1.23	0.71	17.5	9.48	21.16	0.01/1.49
Ga*	ppm	0.1	1	2.5	7.3	10.8	0.4	1.6	0.9	17.5	9.48		0.02/2.69
In	ppm	0.005	0.033	0.006	<0.005	0.037	0.008	0.042	0.015	0.056			0.09/3.39
Tl	ppm	0.02	<0.02	5.62	10.15	1.3	<0.02	<0.02	<0.02	0.9			0.02/11.28
Tl*	ppm	0.5	<0.5	5.7	11.6	1.1	<0.5	<0.5	<0.5	0.9			1.22/12.89
Pb	ppm	0.2	2.4	2	2	5.2	0.6	1.1	0.7	17	2.69	18.33	0.03/0.63
Sn	ppm	0.2	<0.2	0.2	0.2	<0.2	0.4	0.2	0.4	2.1			0.10/1.71
Sn*	ppm	1	<1	<1	<1	<1	<1	1	<1	2.1			0.48/3.33
P	ppm	10	30	170	910	60	20	60	10		1010		/
Bi	ppm	0.01	0.11	0.05	0.02	0.13	0.01	0.37	0.17	0.16	6.2		0.06/2.69
Se	ppm	0.2	<0.2	<0.2	0.4	0.8	<0.2	0.4	<0.2	0.09			4.44/10.00
La	ppm	0.2	4.7	4.9	38.1	47.6	0.8	1.2	3.7	31	0.235	1.87	0.01/1.54
La*	ppm	0.5	4.9	5.9	46.4	46.6	1.1	2.3	7.1	31	0.235		0.04/1.50
Ce	ppm	0.02	5.5	3.35	10.05	5.92	1.09	2.03	6.4	63	0.6	2.38	0.01/0.16
Ce*	ppm	0.5	5.9	4.6	13.3	6.1	1.4	3.7	11.4	63	0.6	2.38	0.02/1.18
Pr*	ppm	0.03	0.93	0.73	9.69	11.35	0.16	0.41	1.25	7.1	0.091		0.02/1.60
Nd*	ppm	0.1	3.7	3.2	40.6	47.6	0.6	1.6	4.2	27	0.464	1.9	0.02/1.76
Sm*	ppm	0.03	0.87	0.86	8.43	13.2	0.11	0.29	0.69	4.7	0.153	0.25	0.02/2.81
Eu*	ppm	0.1	0.48	0.28	3.62	5.52	0.07	0.09	0.2	1.0	0.059	0.17	0.075/5.52
Gd*	ppm	0.05	1.25	0.68	8.67	9.49	0.1	0.29	0.59	4.0	0.206	0.25	0.03/2.37
Tb*	ppm	0.01	0.19	0.12	1.08	1.24	0.01	0.03	0.08	0.7	0.038		0.01/1.77
Dy*	ppm	0.05	1.12	0.71	5.49	5.2	0.06	0.25	0.5	3.9	0.254		0.02/1.41
Ho*	ppm	0.01	0.2	0.15	0.97	0.78	0.01	0.06	0.1	0.83	0.057		0.01/1.22
Er*	ppm	0.03	0.5	0.45	2.59	1.85	0.04	0.25	0.29	2.3	0.166		0.02/1.19
Tm*	ppm	0.01	0.05	0.04	0.35	0.27	<0.01	0.04	0.04	0.30	0.026		0.03/1.80
Yb*	ppm	0.03	0.35	0.31	2	1.51	0.04	0.24	0.26	2.0	0.168	0.15	0.02/1.31
Lu*	ppm	0.01	0.04	0.05	0.3	0.22	0.01	0.03	0.03	0.31	0.025	0.02	0.03/1.23
Eu/Eu*	ppm	1.41	1.12	1.29	1.51	2.04	0.95	0.96					
Ce/Ce*	ppm	0.54	0.35	0.13	0.06	0.59	0.73	0.74					
Σ REE		18.03	16.25	130.7	139.9	3.54	8.68	25.43					
Σ HREE		2.45	1.83	12.78	11.07	0.17	0.9	1.3					
Σ REE		20.48	18.08	143.5	150.9	3.71	9.58	26.73					5.27

DISCUSSION

At the coarse saprolite occurs an early stage of the oxidation process. The oxidation of magnetite has resulted in the replacement of the octahedral structure of the magnetite by hematite. The planes (111) (Graig & Vaughan 1981) controls the substitution in both iron oxides. Different stages of substitution can be seen along the profile, commonly taking place from the edges towards the center of the crystals, with the process being popularly known as "martitization" (Davis *et al.* 1968, Varajão *et al.* 1996). The substitution can be easily identified because of the large amount of magnetite, which remains in the center of the crystals (fig. 14A). More advanced stages occur at the fine saprolite, where the magnetite may be reduced to "islands". Complete replacement of magnetite is often difficult to distinguish at the FS and crusts unless vestigial structures, such as the typical octahedral crystal morphology, which is left behind, resulting in pseudomorphic hematite after magnetite (psh, fig. 14B-D).

The dissolution of quartz and amorphous SiO₂ by weathering conditions was identified as one of the main processes concurring on this profile. The decomposition of quartz, carbonate, and manganese hydroxide has formed spherical to elongated centimeter-long cavities (fig. 14B-D), as a result of the extensive dissolution of those species from the coarse saprolite into the ores. Otherwise, the structure of the original lodging remains up to the crust (Costa & Araújo 1997, Costa *et al.* 2011). The dissolution of Si-minerals is a slow chemical process, via adsorption of water molecules on the surface of these minerals resulting in further formation of four silanol groups around the silicon atom and the detachment of the molecules of orthosilicic acid from the surface (White & Buss 2014, Zhu *et al.* 2017). According to Sokolova (2013), at the final stage of the hydrolysis reaction, the atom of Si surrounded by four OH groups, i.e. the orthosilicic acid H₄SiO₄, is released into the solution. The rates of quartz dissolution at pH 7 and 3 constitute 10^{-15.72} and 10^{-16.12} mol/m² s, respectively (Sokolova 2013).

There are frequent evidences of the bedding collapse (fig. 14B-C), due to the dissolution process of the original jasper bands, associated with intense fracturing, the loss of rock volume may reach up to 40% (Taylor *et al.* 2001, Varajão *et al.* 1996). The collapsed fragments are composed of hematite iron bands with high porosity. They exhibit lateral continuity (fig. 14C) in macro and microscale, which could be considered as an evidence of their ancestry with the jaspilite. Primary hematite shows no evidences of modification along the S11D profile, as expected since this mineral is stable in many environmental conditions (Soumya *et al.* 2011), occurring as microplaty (mpl) hematite (fig. 14D-F), which characterizes the best hematite-rich

ore. The origin of microplaty hematite is still subject of debate. In this work, it is attributed to a primary supergene ore modified by secondary hydrothermal events.

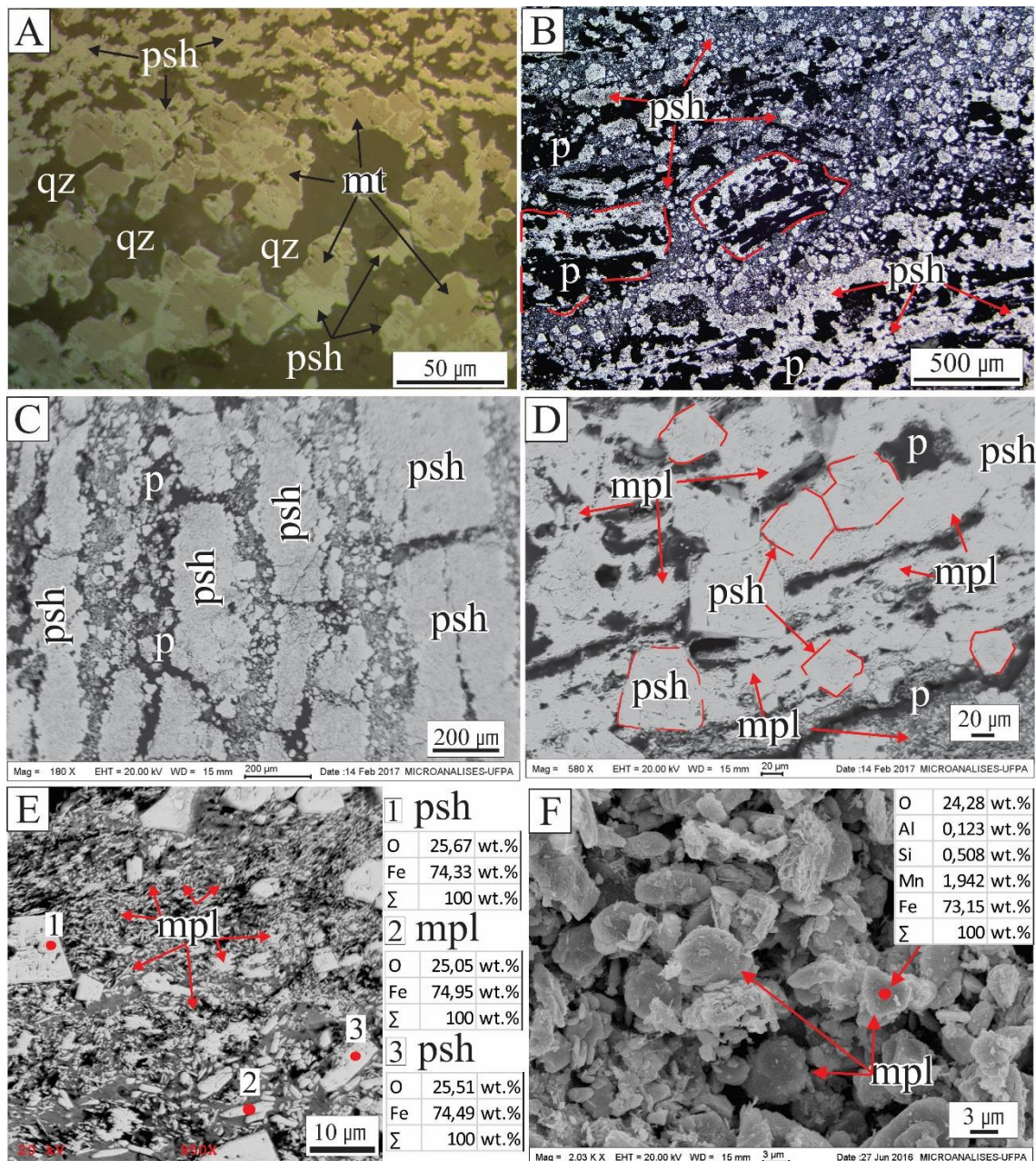


Figure 14- Iron oxides dissolution textures. A-B) Jaspilite, euhedral light-colored crystals of magnetite and quartz (dark); B-C) fragments of opaque ancient banding and elongated porosity; D-F) crystals of pseudomorph hematite after magnetite and microplaty hematite; Photomicrographs on reflected light (A-B) and on SEM by retro-diffused electron (C-E) and secondary electron (F). Magnetite (mt), quartz (qz), pseudomorph hematite after magnetite (psh), goethite (gt), microplaty hematite (mpl) and porosity (p).

The goethite texture ranges from firmly indurated brown material to very friable yellow ochre. The brown goethite is formed by concentric layers of a radial acicular goethite, which may have termination suggestive of rhombohedral or rhombic forms (fig. 15A-C), deposited as a dark brown film on the walls of cavities. The formation of goethite may be related to the high mobility of organometallic complexes of iron and aluminum through water percolation (Tardy & Nahon 1985). The source of iron is the ancient amount of Fe-minerals of the jaspilite: on the jasper bands (microcrystalline quartz with surficial hematite pellicle), and on the magnetite grains (fig. 15E) decomposed by microbial action. The colloids (Bosch *et al.* 2010) would be locally precipitated (fig. 15C) as ferrihydrite ($\text{Fe}_2\text{O}_3 \cdot 0.5\text{H}_2\text{O}$), because of meteoric water circulation (Graig & Vaughan 1981), and subsequently transformed into goethite (FeOOH) (Soumya *et al.* 2011), assuming a botryoidal form.

Iron ores may show some impurities related to MnO , SiO_2 , Al_2O_3 , and P_2O_5 found locally at S11D deposit. The cut-off grade used for the iron ore is normally 60 wt. % Fe, 2 wt.% Mn, 2-2.5 wt.% Si and Al, and 0.2 wt.% P (Figueiredo e Silva *et al.* 2011). According to CVRD (1996), the contaminants are found: (i) in contact with “canga” (aluminum and phosphorous); (ii) in contact with lower basaltic wall rocks (manganese, particularly); and (iii) increasing with depth generally, silica. The newformed minerals at the “canga”, as Al-goethite (fig. 15C, F) and gibbsite, may contribute to the deleterious aluminum for the iron ore (0.05 wt.% to 16.2 wt.%), as well as P in probable aluminum-phosphates (0.01 wt.% to 1.68 wt.% P_2O_5). Primary cryptomelane and hollandite (fig. 14F) could be related to the original stratigraphic variation in the jaspilite composition (Costa 2015, Costa *et al.* 2005, Costa *et al.* 2013, Requelme 2013) and be the major carrier of Mn at the coarse saprolite.

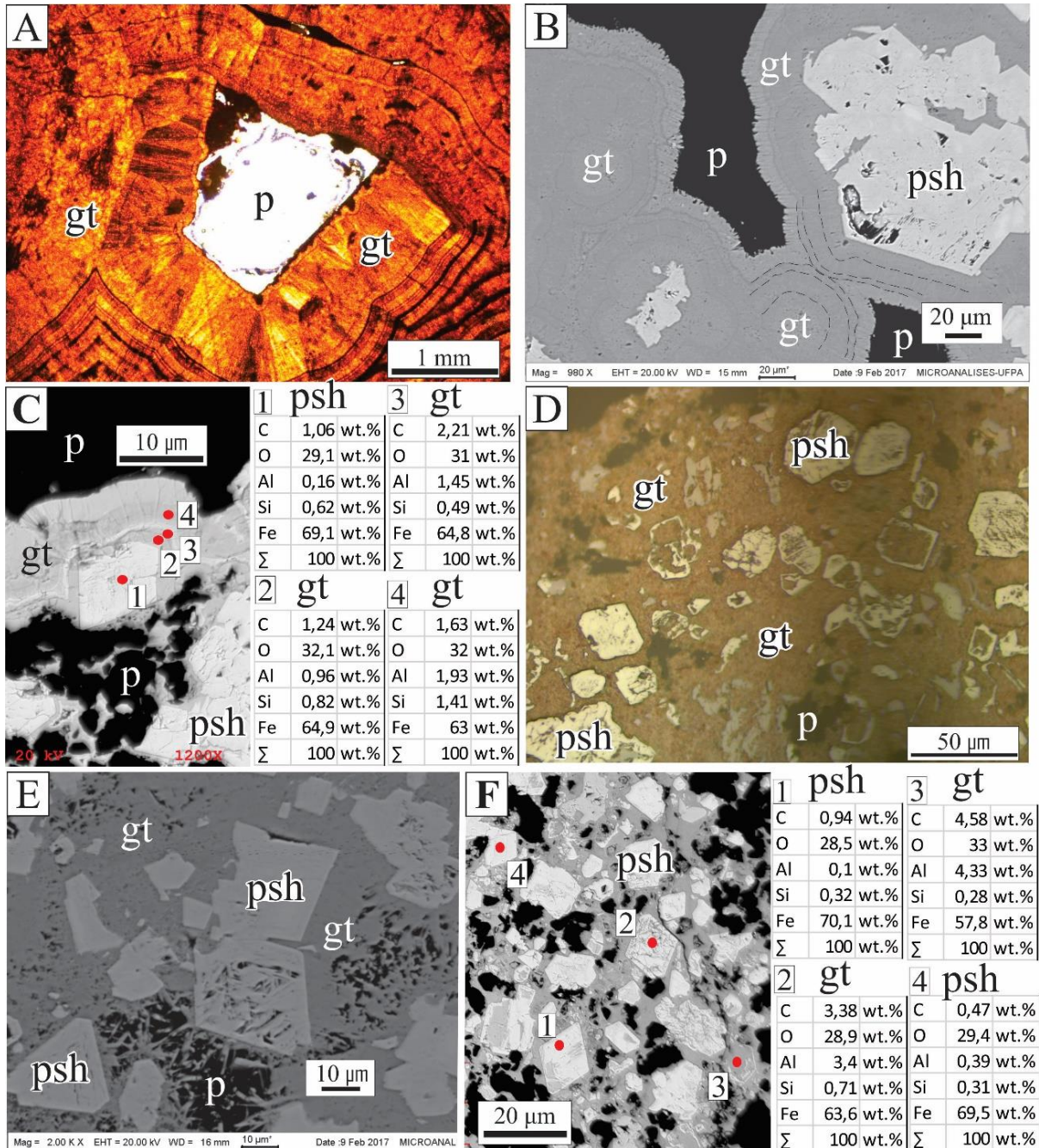


Figure 15- Iron oxides replacement textures. A-C) Concentric banding of fibrous, acicular to rods goethite crystals; C) the banding is concentric towards the porosity center; EDS microanalyses demonstrate variation on the layers composition, headed by Fe, Al and Si; D-E) pseudomorph hematite crystals after magnetite exhibit corroded bounders and sharp or rounded edges; D) goethite cement has filled the ghost crystals; E) most pseudomorph hematite crystals have been dissolved along preferential planes; F) EDS microanalyses of different dissolution stages of pseudomorph crystals demonstrate gradual input of Al depending on the amount of cement inside of the grain. Photomicrographs on plan polarized light (A), on reflected light (D) and on SEM by retro-diffused electron (B-C, E-F). Pseudomorph hematite after magnetite (psh), goethite (gt), and porosity (p).

The distribution of the main chemical components supports the mineralogy. According to Schellmann (1986), the SiO_2 , Fe_2O_3 and Al_2O_3 triplot method uses the major oxides for classifying the weathering products, and compares them to the protore composition, determining the degree of alteration occurring within a laterite weathering profile. This method quantifies three levels of lateritisation, where two main groups have been differentiated with similar compositions for the S11D samples: the BIFs and the ore (fig. 16). The BIF and coarse saprolite samples took place in the field between weak and moderate weathered levels, while the ores (fine saprolite) in the strong weathered.

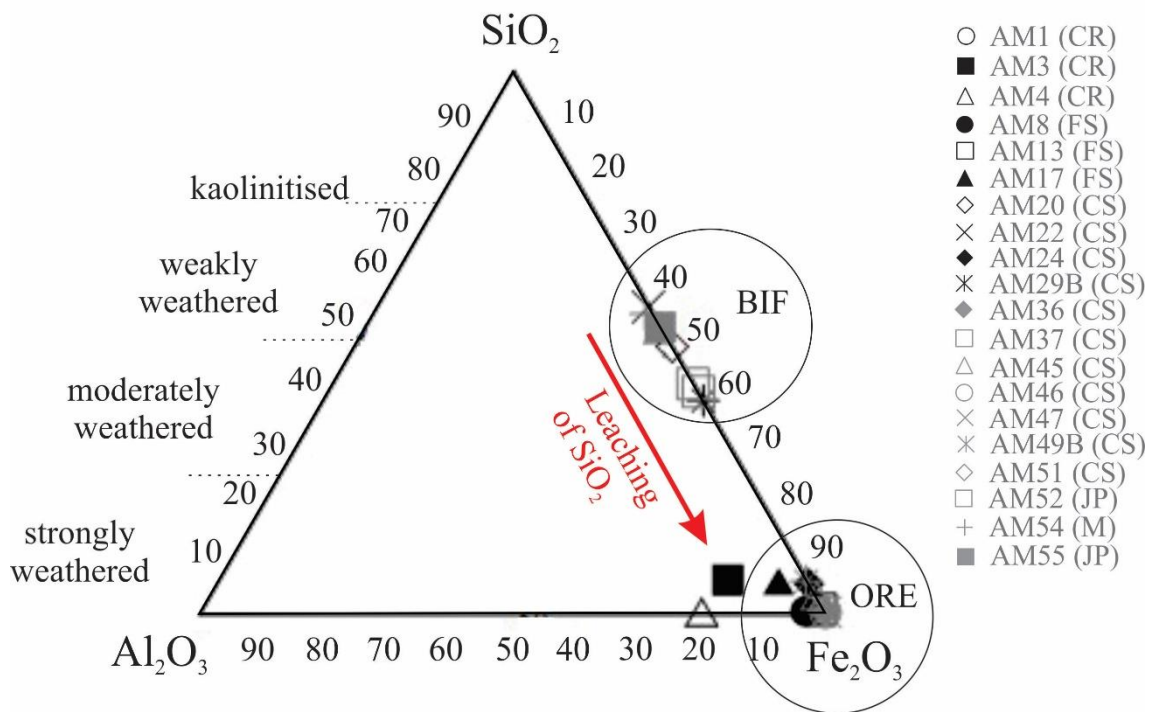


Figure 16- Tri-plot (SiO_2 , Fe_2O_3 , Al_2O_3) of S11D samples data. Circle areas correspond to the determined range of BIF protore composition. Limits of lateritisation for typical laterite profile determined according to the calculation of Schellmann (1986). CR – crust; FS – fine saprolite; CS – coarse saprolite; JP – jaspilite; M – mafic rock.

The mobility of the chemical elements through the regolith has been based on the normalization of their content values from the average of the upper continental crust (UCC, after Rudnick & Gao 2003) and BIF average composition (after Macambira & Schrank 2002) (table 2). According to Costa *et al.* (2014), absolute enrichment is defined for elements with factors that exceed the maximum values recorded for Al (3.0) and Ti (2.8) plus 50%, i.e., 4.5 and 4.2, respectively. Factors 1 to 4.5 correspond to relative enrichment (precipitation in situ), <1.0 to leaching, and absolute enrichment to factor up to 10.1 (Costa *et al.* 2014). Considering these factors, Fe_2O_3 is the only main chemical element with a mobile behavior, as it was

captured locally, related to the impregnation of the newformed goethite on the iron crust and in many parts of the saprolite. Al_2O_3 and TiO_2 are immobile (factor approximately 4.0), denoting a relative enrichment (residual), whereas SiO_2 is mobile (plus MgO , CaO , Na_2O , and K_2O), having leached out of the laterite profile, from the protore into the fine saprolite (FS) and crust (CR). The locally high content of Al and P may be related to the decomposition of mafic dikes (Costa *et al.* 2013) through the regolith, which are probably the main source to the formation of kaolinite, gibbsite, and Al-goethite.

The trace elements Co, Ni, Cu, Cd, and Zn are depleted on the FS and CR. Moreover, they show a positive correlation for $\text{Ni} \times \text{S}$ ($r = 0.30$), $\text{Ni} \times \text{Mo}$ ($r = 0.69$), $\text{Ni} \times \text{Cr}$ ($r = 0.42$) on the protolith samples. It seems reasonable to assume that sulfides from the mafic rocks are the most probable source of those mobile elements, though other host phases cannot be ruled out. When they are mobilized, can form oxyanions in solution, which would be readily adsorbed on protonated Fe oxy-hydroxide surfaces at the low pHs expected to prevail in the oxidizing weathering environment (Dixit & Hering 2003, Mitsunobu *et al.* 2010, Rovira *et al.* 2008, Stollenwerk 2003).

The granitophile elements (Mo, W, U, and Sn) are enriched on the FS and CR (fig. 11, 12) for the S11D samples, while for the BIFs of Carajás (Macambira & Schrank 2002), they are most under the detection limits. This complex signature of the trace elements within the iron oxides could be the result of the impact of the local settings (granite intrusions, ~1.8Ga) over the BIFs (Dall'Agnoll & Oliveira 2007).

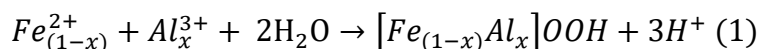
REE, Th, U, Y, Hf, Ta, Nb, Sc, and Zr show a strong positive correlation within each other. They are commonly related to the residual minerals (i.e. zircon - fig.10B and anatase – fig. 10F), which are insoluble and normally immobile under surface conditions (Jiang *et al.* 2005, Santos *et al.* 2016). Furthermore, the distribution curves of the normalized values of REE to the chondrites (fig. 13) show the geochemical signature of jaspilites (Macambira & Schrank 2002). This parallelism between the samples suggests that the horizons hold a strong chemical affinity with the BIFs, indicating that their formation is also strongly connected. Eu shows strongly pronounced positive anomalies in most of the samples. Positive anomalies can be explained by intense surface weathering caused in a strongly oxidizing environment, where most LREE are preferentially removed (McDaniel *et al.* 1994). Ce is removed less readily from the system when oxidized to Ce^{4+} , because it is incorporated into insoluble hydroxides and oxides i.e. cerianite (Braun *et al.* 1990).

THE GENESIS MODEL OF LATERITIC-SUPERGENE IRON ORE AT S11D DEPOSIT, CARAJÁS PROVINCE

The dissolution of jasper and chert bands was possibly the first stage of weathering to the formation of the iron ore (fig. 17A). Molecules of water are adsorbed on the silanol solid surface, causing the release of the orthosilicic acid (H_4SiO_4) into the solution (Sokolova 2013).

The dissolution of quartz species, followed by oxidation of magnetite (fig. 17B), has given residual concentrates of Fe oxides, which has produced a range of porous ore types (fig. 17C). The ore quality ranges from residues of pseudomorphic hematite after magnetite (oxidized magnetite = hematite) \pm primary hematite (microplaty hematite).

The input of small amounts of alumina, from the weathered mafic dykes, into this Fe–Si system may have caused significant modifications in the weathering profile. The most significative expression occurs on the top of the fine saprolite horizon, which have a suite of aluminous minerals (goethite, kaolinite and gibbsite) covering the orebody. The weathered dykes probably help to increase the volume of water percolating through the profile and in turn accelerate the rate of quartz dissolution (fig. 17B). In contrast, apparently the primary iron oxides near the dykes are no more weathered than their counterparts distant from them; that is, the increase in water flow cannot explain, by itself, the more intense weathering of the primary oxides (Ramanaidou 2009). Thus, it appears that alumina plays a key role in the weathering of the primary iron oxides by increasing their dissolution rate (Ramanaidou 2009). Where the solutions are depleted in aluminum, the pseudomorphic hematite grains are possibly dissolved at a slow rate (Ramanaidou 2009), as it occurs at the coarse saprolite, where only limited amounts of secondary aluminum-rich goethite occur. Conversely, where alumina is incorporated into the system, the dissolution of pseudomorphic hematite grains is accelerated (Morris & Ramanaidou 2007, Ramanaidou 2009, Ramanaidou *et al.* 2003), as observed in the fine saprolite and crust horizons. In this iron-rich environment, small amounts of aluminum strongly enhance the weathering by precipitating gibbsite and by combining with iron to form secondary aluminum-rich goethite (Ramanaidou 2009). When gibbsite precipitates from aluminum rich solution, it releases protons (equation 1) generating a local acidic environment, where primary iron oxides dissolve releasing iron cations to the solution, which in turn combines with aluminum to form aluminum-rich goethite (equation 1, Ramanaidou 2009). Gibbsite $[Al(OH)_3]$ is probably the catalyst of the dissolution of the primary iron oxides in a lateritic profile (Ramanaidou 2009).



Near the surface, the dissolution of silica minerals leaves a friable residue of amorphous silica, which is readily eroded (fig. 17B-C), exposing further material for reaction. Thus, the ore body grows upward, as erosion removes the surface which forms a topographic low. The weathering of the jasper bands forms a typical hard cap (iron crust) on the surface of the deposit (fig. 17D), which gives the resistance to erosion, while at the depth, groundwater movement leached the silica to produce porous ore. The typical plateaus of the deposits today are a result of the resistance to erosion of iron crust.

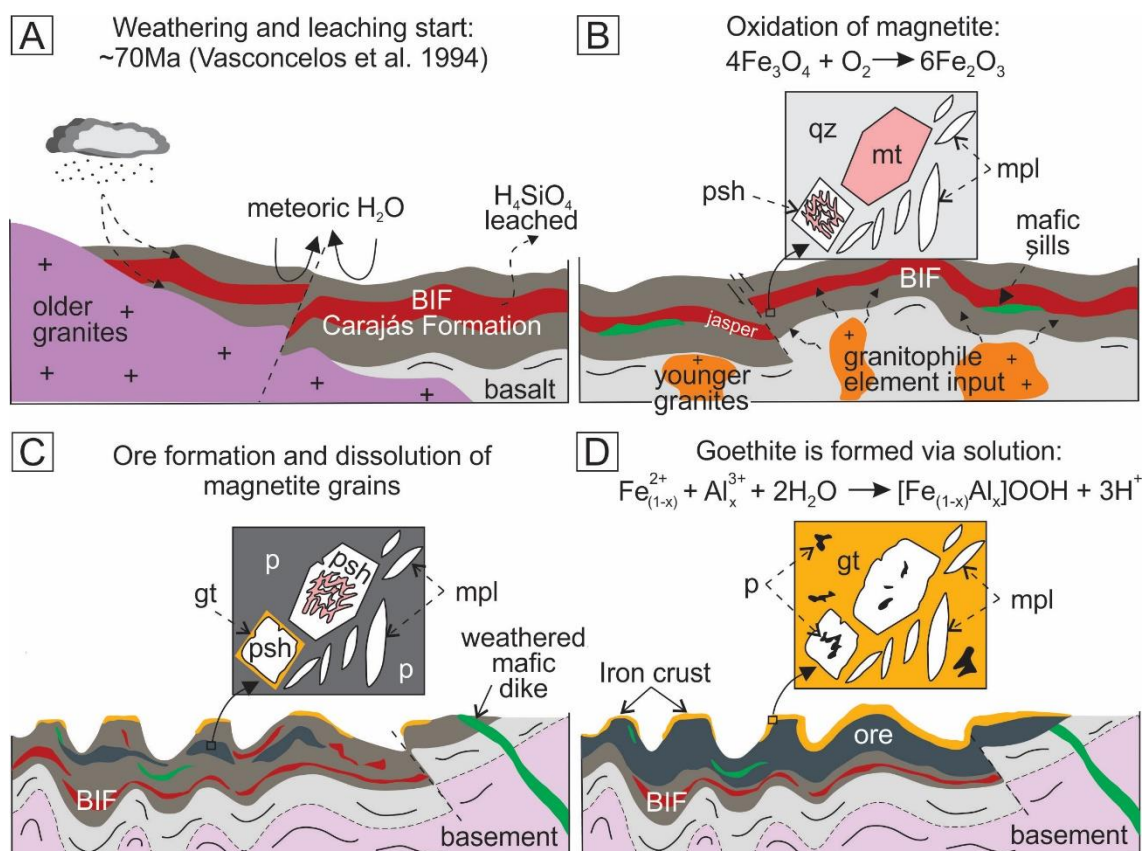


Figure 17- Genesis model of lateritic-supergene iron ore in the Carajás Province. Magnetite (mt), quartz (qz), pseudomorph hematite after magnetite (psh), goethite (gt), microplaty hematite (mpl), and porosity (p).

CONCLUSIONS

The genesis of jaspilite-derived lateritic iron ores of S11D mine consists essentially of dissolution of jasper/chert bands, oxidation, goethitisation, and residual enrichment of iron. The weathering history starts with the coarse saprolite horizon in which the initial parent rock volume is preserved. The leaching of jasper bands is progressive and the goethitisation rate is moderate. Weathering is subtractive and iron enrichment is relative. While quartz is almost completely leached from the protore upwards the crust, in the coarse saprolite horizon, a pseudomorphic replacement of magnetite occurs. The iron crust caps the weathering profile, containing hematitic grains in a goethitic cement. The top of the fine saprolite horizon is rich in iron and aluminum complexes, where the primary structure of jaspilites has been destroyed. The alumina influx is greatly favored by the dykes on the lateritic process. Alumina plays the role of accelerator the process of degradation in this iron-rich environment. In both direct and indirect ways, alumina improves the orebody on the one hand and degrades it on the other. The explanation of the accelerator effect of alumina might be expanded to lateritic profiles overlying other types of bedrocks, since aluminous bedrocks are generally more deeply and rapidly weathered than less aluminous rocks.

The complete sequence of the iron ore studied in S11D, which comprises a complete mature laterite profile, can be well correlated with other iron ore-bearing lateritic profiles that cover the Amazon, and some of the classics expositions in Australia, India and Africa. The best examples in Carajás being those from N8, N5, N4, and N1 deposits. This relationship suggests that these sequences have possibly experienced a similar genesis and evolution.

ACKNOWLEDGEMENT

This research received financial support from CNPq (M.L.C. – grant number 304.519/2009-0 and A.C.S.S. – scholarship), from INCT-GEOCIAM (M.L.C. – grant number - 573733/2008-2), and from ITV-UFPA/FADESP (M.L.C. – grant number – 3753). The authors wish to acknowledge Vale S. A. for providing access to geological data and for the technical, logistic and financial support. We are grateful to the laboratories of Mineral Characterization and Microanalyses at the Geoscience Institute (UFPA). The first author particularly would also like to thank Clovis Maurity (ITV) for his help, assistance, encouragement and innumerable discussions.

7 CONSIDERAÇÕES FINAIS

A gênese do minério de ferro laterítico derivado de jaspilito da mina de S11D, consiste essencialmente na dissolução de jaspe/chert, na oxidação, na goethitização e no enriquecimento residual de óxidos de ferro. O histórico de intemperização começa com o horizonte saprolito grosso em que o volume inicial de rocha parental é preservado. A lixiviação do jaspe é progressiva e a taxa de goethitização é moderada. O intemperismo é subtrativo e o enriquecimento de ferro é relativo. Enquanto, o quartzo é quase completamente lixiviado do protominério em direção a crosta, ocorre uma substituição pseudomórfica da magnetita. A crosta capeia o perfil de intemperismo, contendo grãos de hematita em um cimento de goethita. O topo do horizonte saprolito fino é rico em alumínio, onde a estrutura primária dos jaspilitos foi destruída. O influxo de alumínio é favorecido pela proximidade de diques maficos intemperizados. Alumina desempenha o papel de acelerar a degradação dos óxidos de ferro neste ambiente. De maneira direta e indireta, a alumina melhora o corpo de minério, por um lado, e o degrada por outro. A explicação do efeito acelerante da alumina pode ser expandida para perfis lateríticos que cobrem outros tipos de rocha parental, uma vez que as rochas portadoras de alumínio são geralmente mais profundamente e rapidamente intemperizadas que as rochas menos aluminosas.

A sequência completa do minério de ferro estudado no S11D, que compreende um perfil laterítico maturo completo, pode ser correlacionada com outros perfis lateríticos de minério de ferro que cobrem a Amazônia e algumas exposições clássicas na Austrália, Índia e África. Os melhores exemplos em Carajás são os dos depósitos N8, N5, N4 e N1. Esta relação sugere que essas sequências experimentaram possivelmente uma gênese e evolução similar.

REFERÊNCIAS

- Ab'saber A.N. 1986. Geomorfologia da região. In: Almeida, J.M.G (org.). Carajás: desafio político, ecologia e desenvolvimento. CNPq, Brasília, p. 88-124.
- Barat J., Zanda B., Moynier F., Bollinger C., Liorzou C. 2012. Geochemistry of CI-chondrites: major and trace elements and Cu and Zn isotopes. *Geochimica et Cosmochimica Acta*, **83**: 79-92.
- Bosch J., Heister K., Hofmann T., Meckenstock R.U. 2010. Nanosized iron oxide colloids strongly enhance microbial iron reduction. *Appl. Environ. Microbiology*, **76**: 184-189.
- Braun J.J., Pagel M., Muller J.P., Bilong P. Michard A., Guillet B. 1990. Cerium anomalies in lateritic profiles. *Geochimica et Cosmochimica Acta*, **54**: 781-795.
- Cornell R. M. & Schwertmann U. 1996. *The iron oxide*: structure, properties, reactions and uses. Second edition. Weinheim, Wiley-VCH GmbH & Co. KGaA.
- Costa L. C. 2015. *Minerais de manganês como contaminantes do minério de ferro na mina N5W em Carajás, Pará*. MS Dissertation, Instituto de Geociências, Universidade Federal do Pará, Belém, 87p.
- Costa M.L. 1991. Aspectos geológicos dos lateritos da Amazônia. *Revista Brasileira de Geociências*, **21** (2): 146-160.
- Costa M. L. & Araújo E. S. 1997. Caracterização mineralógica e geoquímica multi-elementar de crostas ferruginosas lateríticas tipo minérios de ferro em Carajás. São Paulo. *Geociências*, **16** (1): 55-86.
- Costa M.L., Carmo M. S., Behling H. 2005a. Mineralogia e geoquímica de sedimentos lacustres com substrato laterítico na Amazônia Brasileira. *Revista Brasileira de Geociências*, **35** (2): 165-176.
- Costa L. C. G., Costa M. L., Farias H. D., Couto A., Galbiatti F., Braga M. A. S. 2013. Os minerais contaminantes do minério de ferro de N5W, Carajás-PA: oxi-hidróxidos de Mn e sílica. In: SBG, 13º Simpósio de Geologia da Amazônia. *Recursos minerais e sustentabilidade territorial na Amazônia: anais – resumos expandidos*. Cap. 7, p. 671-674.
- Costa M. L., Cruz G. S., Almeida H.D.F, Pollmann H. 2014. On the geology, mineralogy and geochemistry of the bauxite-bearing regolith in the lower Amazon basin: evidence of genetic relationships. *Journal of Geochemical Exploration*, **146**: 58-74.
- Costa M.L., Fernandez O. J. C., Requelme M. E. R. 2005b. O Depósito de Manganês do Azul, Carajás: estratigrafia, mineralogia, geoquímica e evolução geológica. In: Caracterização de depósitos minerais em distritos mineiros da Amazônia. ADIMB. p. 227-334.
- Costa M. L., Leite A.S., Poellmann H. 2016. A laterite-hosted APS deposit in the Amazon region, Brazil: the physical-chemical regime and environment of formation. *Journal of Geochemical Exploration*, **170**: 107-124.
- Costa M. L., Queiroz J. D. S., Silva A. C. S., Almeida H. D.F., Costa L. C.C. 2011. Perfil Laterítico Desenvolvido Sobre Formação Ferrífera Bandada (Jaspilito) em Carajás. In: SBG, 12º Simpósio de Geologia da Amazônia, *Anais... Boa Vista, Roraima*, p. 403-407.
- Costa M. L., Sousa D. J. L., Angélica R. S. 2009. The contribution of lateritisation processes to the formation of the Kaolin deposits from Eastern Amazon. *Journal of South American Earth Sciences*, **27**: 219-234.

- Companhia Vale do Rio Doce. 1996. Resumo dos aspectos geológicos da Província Mineral Carajás, in Guia de excursão: DIGEB/DEPAB/ GIMB/SUMIC, p. 392-403.
- Dall'Agnol R., Oliveira D.C., 2007. Oxidized, magnetite-series, rapakivi-type granites of Carajás, Brazil: Implications for classification and petrogenesis of A-type granites: *Lithos*, **93**: 215–233.
- Dall'agnol R., Oliveira D.C., Guimarães F.V., Gabriel E.O., Feio G.R.L., Lamarão C.N., Althoff F.J., Santos, P.A., Teixeira M.F.B., Silva A.C., Rodrigues D.S., Santos M.J.P., Silva C.R.P., Santos, R.D., Santos P.J.L., 2013. Geologia do Subdomínio de Transição do Domínio Carajás – Implicações para a evolução arqueana da Província Carajás - Pará. In: 13º Simpósio de Geologia da Amazônia. CD rom, Anais, Belém (in Portuguese).
- Dalstra H., Guedes S. 2004. Giant hydrothermal hematite deposits with Mg-Fe metasomatism: a comparison of the Carajás, Hamersley and other iron ores. *Economic Geology*, **99**: 1793-1800.
- Davis B.L., Rapp Jr. G., Walawender M.J. 1968. Fabric and structural characteristics of the martitization process. *American Journal Science*, **266**:482-496.
- Dixit S. & Hering J. G., 2003, Comparison of arsenic(V) and arsenic(III) sorption onto iron oxide minerals: Implications for arsenic mobility: *Environmental Science and Technology*, **37**: 4182-4189.
- Figueiredo E Silva R. C.; Lobato L. M., Rosière C. A., Hagemann S. 2011. Petrographic and geochemical studies at giant Serra Norte iron ore deposits in the Carajás mineral province, Pará State, Brazil. *Geonomos*, **19** (2): 198-223.
- Figueiredo E Silva R.C., Lobato L.M., Rosière C.A., Hagemann S.G, Zucchetti M., Baars F.J., Morais R., Andrade I. 2008. Hydrothermal origin for the jaspilite-hosted, giant Serra Norte iron ore deposits in the Carajás mineral province, Para State, Brazil. In: Hagemann, S.G., Rosière, C.A., Gutzmer, J., and Beukes, N.J. (eds.), BIF-related high-grade iron mineralization. Reviews in *Econ. Geo.*, **15**: 255-290.
- Figueiredo E Silva, R. C., Hagemann, S., Lobato L. M., Rosière C. A.; Banks D. A., Davidson G. J., Vennemann T., Herdt J. 2013. Hydrothermal Fluid Processes and Evolution of the Giant Serra Norte Jaspilite-Hosted Iron Ore Deposits, Carajás Mineral Province, Brazil. *Economic Geology*, **108**: 739–779.
- Gibbs A.K., Wirth K.R., Hirata W.K., Olszewski Jr. W.J., 1986. Age and composition of the Grão Pará Group volcanics, Serra dos Carajás. *Rev. Bras. Geoc.* **16**:201–211.
- Grainger C.J., Groves D.I., Tallarico F.H.B., Fletcher I.R. 2008. Metallogenesis of the Carajás Mineral Province, southern Amazon Craton, Brazil: Varying styles of Archean through Paleoproterozoic to Neoproterozoic baseand precious-metal mineralization. *Ore Geology Reviews*, **33**: 451-489.
- Hirata W.K., Rigon J.C., Kadekaru K., Cordeiro A.A.C., Meireles E.A. 1982. Geologia Regional da Província Mineral de Carajás. In: SBG, Simp. Geol. Amaz., 1, Belém, Anais, 100–110.
- Horbe A. C. & Costa, M. L. 2005. Lateritic crusts and related soils in eastern Brazilian Amazonia. *Geoderma* (Amsterdam), **126**: 225-239.
- Jiang S.Y., Wang R.C., Xu X.S., Zhao K.D. 2005. Mobility of high field strength elements (HFSE) in magnetic-, metamorphic-, and submarine-hydrothermal systems. *Phys. Chem. Earth*, **30**: 1020-1029.

- Klein C. & Ladeira E.A. 2002. Petrography and geochemistry of the least-altered banded iron-formation of the Archean Carajás Formation, northern Brazil. *Economic Geology*, **97**: 643-651.
- Lasaga A. C. & Gibbs G. V. 1990. Ab Initio Quantum Mechanical Calculations of Water–Rock Interactions: Adsorption and Hydrolysis Reactions. *Am. J. Sci.*, **290**: 263–295.
- Macambira J.B. 2003. *O ambiente deposicional da Formação Carajás e uma proposta de modelo evolutivo para a Bacia Grão Pará*. PhD Thesis, Instituto de Geociências, Universidade Estadual de Campinas, São Paulo, 217p.
- Macambira J.B. & Schrank, A. 2002. Químico-estratigrafia e evolução dos jaspilitos da Formação Carajás (PA). *Revista Brasileira de Geociências*, **32**: (4), 567-577.
- Meirelles M.R. 1986. *Geoquímica e petrologia dos jaspilitos e rochas vulcânicas associadas, Grupo Grão-Pará, Serra dos Carajás*. MS Dissertation, Universidade de Brasília, 171p.
- Mcdaniel D.K., Hemming S.R., McLennan S.M., Hanson G.N. 1994. Resetting of neodymium isotopes and redistribution of REEs during sedimentary processes: The Early Proterozoic Chelmsford Formation, Sudbury Basin, Ontario, Canada. *Geochimica et Cosmochimica Acta*, **58**: 931-941.
- McLennan S.M. 1989. Rare Earth Elements in Sedimentary Rocks: Influence of Provenance and Sedimentary Process. *Review of Mineralogy*, **21**: 169-200.
- Mitsunobu S., Takahashi Y., Terada Y., Sakata M. 2010. Antimony(V) incorporation into synthetic ferrihydrite, goethite, and natural iron oxyhydroxides. *Environmental Science & Technology*, **44**: 3712-3718.
- Morris R.C. & Ramanaidou E.R., 2007. Genesis of the channel iron deposits (CID) of the Pilbara region, Western Australia. *Australian Journal of Earth Sciences*, **54**: 733–756.
- Oliveira S.B., Costa M.L., Prazeres Filho, H.J. 2016. The Lateritic Bauxite Deposit of Rondon do Pará: A New Giant Deposit in The Amazon Region, Northern Brazil. *Economic Geology and the Bulletin of the Society of Economic Geologists*, **111**: 1277-1290.
- Radam 1974. Projeto Radam Brasil: Folha SB.22 Araguaia e parte de SC.22 Tocantins; geologia, geomorfologia, pedologia, vegetação e uso potencial da Terra. Programa de Integração Nacional, Levantamento de Recursos Naturais, 4, Rio de Janeiro.
- Ramanaidou E. R. 2009. Genesis of lateritic iron ore from banded iron-formation in the Capanema mine (Minas Gerais, Brazil), *Australian Journal of Earth Sciences*. **56** (4): 605-620.
- Ramanaidou E. R., Morris R. C., Horwitz R. C. 2003. Channel iron deposits of the Hamersley Province, Western Australia. *Australian Journal of Earth Sciences*. **50**: 669–690.
- Requelme M. E. R. 2013. *Mineralogia e Química-Mineral dos Oxi-hidróxidos de Manganês do Depósito do Azul, Província Mineral de Carajás: A Importância da Série Criptomelana-Hollandita*. PhD Thesis, Instituto de Geociências, Universidade Federal do Pará, Belém, 173p.
- Rudnick R.L. & Gao, S. 2003. Composition of the continental crust. In: Rudnick, R.L., Holland, H.D. and Turekian, K.K. (eds). *The Crust. Treatise on Geochemistry*, 3, Amsterdam, Elsevier, p. 1-64.
- Santos P. H. C., Costa, M.L., Leite, A.S. 2016. The Piriá aluminous lateritic profile: mineralogy, geochemistry and parent rock. *Brazilian Journal of Geology*, **46**: 617-636.
- Schaefer C. E. G. R., E. Lima Neto G. R. Corrêa F. N. B. Simas J. F. Campos B. A. F. Mendonça B.A.F, Nunes J. A. 2016. Geoambientes, solos e estoques de carbono na Serra Sul de Carajás, Pará, Brasil. *Boletim do Museu Paraense Emílio Goeldi, Ciências Naturais*, **11**(1): 85-101.

- Schellmann W., 1986. A new definition of laterite. In: Banerji, P.K. (Ed.) Lateritisation processes. *Memoir of the Geological Survey of India*, **120**: 1-7.
- Secco R. S. & A. L. Mesquita 1983. Nota sobre a vegetação de canga da Serra Norte - I. *Boletim do Museu Paraense Emílio Goeldi*, Nova Série Botânica, **59**: 1-13.
- Silva M. G. 2014. Metalogênese das províncias tectônicas brasileiras. Organizadores Maria da Glória da Silva, Manoel Barreto da Rocha Neto, Hardy Jost [e] Raul Minas Kuyumjian – Belo Horizonte: CPRM, 2014. 589 p.: il. ISBN 978-85-7499-221-1.
- Soumya D., Hendry J. M., Essilfie-Dugan J. 2011. Transformation of two-Line Ferrihydrite to Goethite and Hematite as a Function of pH and Temperature. *Environ. Sci. Technol.*, **45** (1): 268–275.
- Stollenwerk K. G., 2003, Geochemical processes controlling transport of arsenic in groundwater: a review of adsorption. In: Welch A. H., Stollenwerk K. G. (eds.). Arsenic in Groundwater. Boston: Kluwer Academic Publishers, p. 67-100.
- Tardy Y. & Nahon D. 1985. Geochemistry of laterites stability of Al-goethite, Al-hematite and Fe⁺³-kaolinite in bauxites and ferricretes: An approach to the mechanism of concretion formation. *American Journal of Science*. **285**: 865-903.
- Taylor D., Dalstra H.J., Harding A.E., Broadbent G.C., Barley M.E. 2001. Genesis of high-grade hematite orebodies of the Hamersley Province, Western Australia. *Economic Geology*, **96**: 837-873.
- Taylor S.R. & McLennan S.M. 1985. The Continental Crust: its Composition and Evolution; an examination of the geochemical record preserved in sedimentary rocks. *Blackwell Scientific*, Oxford, 312.
- Tolbert G.E., Tremaine J.W., Melcher G.C., Gomes C.B. 1971. The recently discovered Serra dos Carajás Iron Deposits, Northern Brazil. *Economic Geology*, **66**: 985–994.
- Vale S.A. 2017. Form 20-F. Annual Report Pursuant to Section 13 Or 15(D) of the Securities Exchange Act Of 1934, p. 289.
- Vale S.A. 2018. Annual report of production and sale. Available at: <http://www.vale.com/PT/investors/information-market/Press-Releases/ReleaseDocuments/2017%204Q%20Production%20Report_p.pdf>. Access on: 11th of April, 2018.
- Varajão C.A.C., Ramanaido E., Colin F., Nahon D. 1996. Martitização: alteração supergênica da magnetita. *Revista Escola de Minas*, **50**: 18-20.
- Vasquez L.V., Rosa-Costa L.R., Silva C.G., Ricci P.F., Barbosa J.O., Klein E.L., Lopes E.S., Macambira E.B., Chaves C.L., Carvalho J.M., Oliveira J.G., Anjos G.C., Silva H.R. 2008a. Faltou o título da parte estudada. In: Vasquez M.L. &, Rosa-Costa L.T. (Org.). Geologia e recursos minerais do Estado do Pará: texto explicativo dos mapas geológico e tectônico e de recursos minerais do Estado do Pará: Sistema de Informações Geográficas — SIG, escala 1:1.000.000. Belém: CPRM, 1 CD-ROM.
- Vasquez M.L., Sousa C.S., Carvalho J.M.A. (Orgs.). 2008b. *Mapa geológico e de recursos minerais do Estado do Pará, escala 1:1.000.000*. Programa Geologia do Brasil (PGB), Integração, Atualização e Difusão de Dados da Geologia do Estado do Brasil, Mapas Geológicos Estaduais. CPRM-Serviço Geológico do Brasil, Superintendência Regional de Belém, , 1 CD-ROM.

ANEXOS

ANEXO A- COMPROVANTE DE SUBMISSÃO AO “BRAZILIAN JOURNAL OF GEOLOGY”.

7/2/2018

ScholarOne Manuscripts

The screenshot shows a web-based manuscript submission system. At the top left is a logo for "Brazilian Journal of Geology". To its right are links for "Home" and "Author". The main title "Brazilian Journal of Geology" is displayed prominently. Below it, there's a large button labeled "Submit Manuscript". On the right side of the screen, there's a "Print" button. The overall layout is clean and professional, typical of academic publishing software.

Submission Confirmation

Print

Thank you for your submission

Submitted to

Brazilian Journal of Geology

Manuscript ID

BJGEO-2018-0076

Title

THE CONTRIBUTION OF WEATHERING ON THE GENESIS OF THE IRON ORE AT S11D DEPOSIT, IN CARAJÁS, AMAZON REGION, BRAZIL

Authors

Sousa da Silva, Aline
COSTA, MARCONDES

Date Submitted

02-Jul-2018

Author Dashboard

© Clarivate Analytics | © ScholarOne, Inc., 2018. All Rights Reserved.

ScholarOne Manuscripts and ScholarOne are registered trademarks of ScholarOne, Inc.

ScholarOne Manuscripts Patents #7,257,767 and #7,263,655.

@ScholarOneNews | System Requirements | Privacy Statement | Terms of Use